Energy & Buildings 304 (2024) 113836

Contents lists available at ScienceDirect

Energy & Buildings

journal homepage: www.elsevier.com/locate/enb

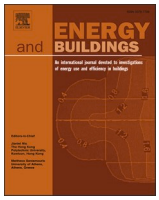

Natural ventilation effectiveness in low-income housing to challenge energy poverty

Roberto Stasi [a,*], Francesco Ruggiero [a], Umberto Berardi [b]

[a] Department of Architecture, Built Environment and Design, Polytechnic University of Bari, Via Edoardo Orabona, 4, 70126 Bari, Italy
[b] Department of Architectural Science, Toronto Metropolitan University, 350 Victoria St., Toronto, Canada

ARTICLE INFO

Keywords:
CFD
Cross-ventilation
Adaptive comfort model
Passive cooling
Natural ventilation
Building form

ABSTRACT

The steady rise in global average temperatures due to climate change is leading to a significant increase in cooling energy demand worldwide. Despite having the least access to energy, the Global South will experience the greatest increase in cooling degree days (CDD), forcing the majority of the world's population to endure highly uncomfortable temperatures in the buildings. As a result, it becomes crucial to prioritize passive design-based approaches to air conditioning, to mitigate the increasing demand for active cooling while ensuring equitable space cooling opportunities for all. This work, combing the CFD simulation with building energy modeling, evaluates the impact of natural cross-ventilation and building form on improving indoor thermal conditions in hot and arid climates. The analysis, focusing on low-income housing prototypes designed by Indian architect Charles Correa, demonstrates how proper building form design, by improving the ventilation and cooling efficiency of buildings, can ensure indoor thermal comfort even in challenging climatic conditions, helping to reduce energy consumption and prevent energy poverty. Natural ventilation provides an operative temperature reduction of up to 3.1 °C on the hottest day and up to 3.9 °C on the typical cooling period day. Even discomfort hours are drastically reduced by 31.3 % and 77.8 % respectively.

1. Introduction

The escalating global average temperatures resulting from global warming [1], along with lengthier periods of intense heat [2] and a higher frequency of extreme events such as heatwaves [3], combined with the growing need for indoor thermal comfort, particularly in Global South developing countries [4], is leading to a remarkable surge in the energy demand for cooling worldwide, as buildings increasingly rely on air conditioning systems [5].

On a global scale, the energy consumption in buildings rose from 115 EJ in 2010 to nearly 135 EJ in 2021, constituting approximately 30% of global final energy usage [6]. After the easing of COVID-19 restrictions, energy demand in buildings surged by approximately 4 % in 2021 compared to 2020, marking the most significant annual increase in the past ten years. Electricity accounted for around 35% of building energy consumption in 2021, with an increasing share for space cooling rose by 6.5% compared to previous year [7].

Projections based on future climate change indicate a potential doubling of current cooling demand in most European countries [8,9]. Even in heating-dominated climates like Canada, an increase of 15 to 126% is expected [10]. However, the most significant increase in energy demand will take place in emerging economies. China is projected to experience an up to 7.5-fold increase in electricity consumption for cooling based on the RCP 4.5 scenario [11]. Brazil's consumption is expected to rise by 70 to 190% by 2100 [12]. In India, a 45% increase is projected as early as 2030 [13]. In particular, the estimated cooling demand for the city of Mumbai alone in India will be almost 24 % of the total cooling demand in the United States [14]. As evaluated by the International Energy Agency (IEA) [15], climate change-driven rising temperatures will outcome an increased use of air conditioning systems. In India, specifically, the demand for cooling energy in buildings may contribute to up to 44% of the country's peak load by 2050 [16]. Increased electricity usage during cooling period has the potential to affect the reliability of the power grid [17]. Consequently, future cooling demand will exacerbate the environmental impact of the building sector and reduce the effectiveness of existing energy-saving and greenhouse gas reduction policies [18].

Furthermore, by 2050, more than 68% of the world's population is expected to live in urban areas, with a significant concentration in the Global South [19]. Most of them will be in developing countries, mainly in tropical regions, which currently have limited access to cooling

* Corresponding author.
E-mail address: Roberto.stasi@poliba.it (R. Stasi).

https://doi.org/10.1016/j.enbuild.2023.113836
Received 6 August 2023; Received in revised form 17 October 2023; Accepted 13 December 2023
Available online 18 December 2023

Nomenclature

ALD	ASHRAE Likehood of Dissatisfied
AC	Air conditioning
ACH	Air Change Rate
BAS	Building Automation System
CDD	Cooling degree days
CFD	Computational fluid dynamics
EC	Energy cost
ED	Energy demand
EP	Energy poverty
IAQ	Indoor Air Quality
IEA	International Energy Agency
IMAC	Indian Model for Adaptive Comfort
INR	Indian Rupee
ISHRAE	Indian Society of Heating, Refrigerating and Air Conditioning Engineers
LiH	Low-income Housing
LPD	Long-term Percentage of Dissatisfied
MM	Mixed-mode ventilation
NV	Natural ventilation
PMV	Predicted Mean Vote
POR	Percentage Outside the Range
RACs	Room Air Conditioners
RANS	Reynolds-Averaged Navier-Stokes
SST	Shear Stress Transport
WD	Wind Driven ventilation

Symbology

h_i	occupancy hour
k	von Karman constant
t_a	average air temperature
t_o	operative temperature
t_r	mean radiant temperature
u^*	friction velocity
u_{ref}	reference wind speed
z_{ref}	reference height
v_r	relative air velocity
ε	turbulence dissipation rate
ω	specific dissipation rate

Fig. 1. Population by country at high risk due to a lack of access to cooling [30].

systems in buildings. It is worth noting that in the hottest areas of the world, only 12 % of households have access to air conditioning, in stark contrast to the over 90% usage rates in the United States and Japan [15]. While Global North countries are increasingly relying on air conditioning as a means to alleviate the impacts of global warming, this option remains unavailable to many. Rising ambient temperatures, coupled with potentially inadequate building design and limited resources for mechanical cooling systems, have resulted in a significant proportion of the world's population - over one billion people - being forced to endure highly uncomfortable indoor temperatures [20].

Amidst global warming, it becomes crucial to prioritize the equitable fulfilment of cooling requirements since air-cooling systems are emerging as the primary safeguard against mortality risk for the most vulnerable segments of society, mitigating the potential health consequences of extreme heat and maintaining thermal comfort within buildings [21–23]. As pointed out by Ebi et al. [24] extreme heat caused an increase of about 356,000 deaths in 2019 alone. In developing countries such as India, where there is a lack of air conditioning, mainly due to economic factors, mortality has been found to increase by more than 18.1% during heatwave periods compared to non-heatwave ones, peaking at 29.9% in regions such as Jaipur [25].

Thus, space cooling is set to become the most widely adopted heat mitigation strategy worldwide, yet it is unaffordable for many of the most vulnerable, financially and environmentally costly, and leaves many defenceless from extreme heat during power outages [26]. As highlighted by Randazzo et al. [27], the increasing importance of cooling systems as an essential need, even in countries that historically haven't relied on such devices, could potentially worsen energy poverty.

Energy poverty is driven by four factors: poverty; high energy prices; energy inefficiency and energy accessibility [28]. As a matter of fact, the concept of energy poverty differs between the Global North and the Global South. In the Global South, the focus shifts towards issues related to accessibility, specifically in rural or developing areas where households lack access to modern energy services rather than to energy efficiency or energy cost [29].

As revealed by the SEforALL (*Sustainable Energy for All*) project [30] across Global South countries at least 3.66 billion people in 2022 face high or medium risk from some type of cooling access challenge (Fig. 1).

Consequently, the economic or physical total lack of energy access, particularly in rural regions of these poorest countries, stresses the importance of exploring alternative approaches to air conditioning to cope with the health risks associated with the inevitable trajectory of climate change and ensure improved indoor comfort conditions [31]. There is an urgent need to prioritize passive, nature-based alternatives to air conditioning, wherever possible, to reduce the surge in cooling demand for active technologies and to ensure equal opportunities to address the consequences of global warming [32,33].

1.1. The role of NV in coping with energy poverty

To adequately cope with the estimated increase in cooling energy demand cost due to global warming, and to effectively design buildings for future challenges, the use of passive cooling methods will be imperative [34,35]. By embracing techniques such as natural ventilation (NV) in buildings, it is possible to achieve acceptable indoor comfort conditions while simultaneously reducing energy demand for active cooling systems and ensuring better indoor air quality (IAQ) [36,37].

Relying on natural forces, NV allows indoor spaces to be cooled down by compensating indoor thermal loads with colder outdoor air, without economic costs as energy consumption is not required [38,39]. Thus, due to its economic and energetic affordability, NV within the buildings has been historically the primary method for passively cooling before the advent of air conditioning systems, and it continues to serve as the sole option for nearly 70% of the global population. Hence, it can still today serve as a vital asset in the pursuit of energy consumption reduction for cooling purposes within buildings, ensuring affordable space cooling for all [40].

Depending on driven natural force, the air movement within the building can be induced by the wind-driven pressure difference, buoyancy phenomenon (also known as stack effect), or concurrently both [41]. Wind-driven ventilation can be classified by openings location into cross-ventilation [42] and single-sided ventilation [43]. Single-sided ventilation (SSV) occurs when one or several openings lay on the same wall, conversely openings on different walls generates cross-ventilation (CR).

Compared to SSV, CV ensures higher ventilation rates and more effective ventilative cooling capacity providing better comfort conditions [44]. As highlighted by Omrani et al. [45] CV is able to provide comfort conditions for the 70% of the time compared to 1% for SSV, ensuring an air change rate 14 times higher than SSV one [46].

Even if NV potential is highly dependent on climatic conditions [47] and may change over time due to global warming [48], the cooling potential of NV strategies is still recognized as one of the key elements for the design of sustainable buildings [49] even when coupled with the mechanical system in mixed-mode ventilation [50,51].

Indeed, NV in buildings offers a wider range of indoor temperatures that are considered comfortable compared to mechanically controlled buildings [52]. This extended comfort range allows the building to be conditioned less frequently and less intensively, resulting in significant reductions in energy consumption and space cooling costs [53,54].

Previous studies on NV have underlined how its implementation in buildings can provide a cooling energy saving up to 50 % depending on local climate [55]. Research by Li et al. [56] showed how cooling demand depending on climate zone 60–100% of the cooling demand can be met by NV, with 35 of the 100 cities observed being fully covered. Even in severe hot climate, such as the Indian one, NV shows an average cooling potential varying between 39% and 78% during the entire year, highlighting how for all climatic zones of India, thanks to NV a significant reduction in the cooling load and energy consumption can be recorded [57].

Even at elevated temperatures, the airflow powered by NV, especially with cross-ventilation, can positively impact the occupants' thermal comfort conditions [58,59]. Along this line, Nicol et al. [60] observed in hot climates air speeds up to 1.5 m/s can be accepted inside the building. Specifically, an ambient air velocity between 0.42 and 0.67 m/s and 0.92–1.08 m/s can ensure an operating temperature drops of 3 °C and 6 °C respectively [61].

Undoubtedly, NV performance in buildings is influenced by many factors including temperature and humidity ratio, the difference between indoor and outdoor environments [62,63], urban surroundings [64–66], windows and doors opening ratio [67], outdoor wind speed [68], and airflow pattern inside the building [69]. Nevertheless, past research has indicated that the way natural ventilation occurs may differ based on occupants involved. This aspect turns Building Automation Systems (BAS) crucial to correctly control and fully benefit NV potential. Along this line, Chen et al. [70] demonstrated how a fully automatic system for NV integrated with predictive control, succeeds in producing an energy savings of 17–80% with zero discomfort degree hours.

Currently, to assess thermal comfort achievable by the NV action and the influence of indoor air velocity the adaptive models are widely accepted as efficient method in naturally ventilated buildings [71,72]. By being adaptable to occupant behaviour and expectations, these models can identify the suitable operating mode to determine when to rely either on natural ventilation or air conditioning, reducing instances of fuel poverty simply by changing operating patterns and reducing household energy costs [73].

1.2. Study methods to assess NV in buildings

In light of the strong dependence of natural ventilation on building form, it becomes priority to conduct a precise evaluation of the architectural configuration and its intrinsic interplay with natural ventilation dynamics. Such an assessment assumes paramount significance for the optimal harnessing of the inherent potential of natural ventilation [74]. NV design for buildings requires in-depth knowledge and accurate prediction of airflow in order to quantify natural ventilation rates and the associated effects on building indoor comfort.

Usually in early design stage, analytical and empirical methods is preliminary used to assess NV within the buildings [41]. These methods, although widely validated by experimentation, remain simplified tools, hence they serve as the primary means to predict overall building ventilation performance. Recent advancements in computational tools, sensors, and data analytics have expanded the possibilities for natural ventilation research, enabling more accurate modeling and real-world validation.

At present, the predominant research methodologies for evaluating NV primarily encompass full-scale measurements, reduced-scale measurements within wind tunnels, and computational fluid dynamics (CFD) simulations [75]. Full-scale experiments involve the collection of real-world data from buildings equipped with natural ventilation systems, offering empirical evidence of system performance and occupant comfort [76]. This approach can be time-consuming and resource intensive. Setting up measurement equipment, data acquisition systems, and monitoring infrastructure for a real building can require a significant financial investment. Furthermore, researchers have limited control over external environmental factors such as wind speed, temperature, and humidity in real-world settings. These uncontrollable variables can introduce variability and uncertainty into the measurements and limit the analysis to a particular building and location, making it difficult to replicate the exact conditions in other studies [77]. Moreover, this method exclusively lends itself to post-occupancy analysis and does not offer substantive guidance during the preliminary building design phase.

Indeed, ventilation systems driven by natural forces must be designed with the building, since the building itself and its spatial elements play a crucial role in either reducing or increasing the air movement affecting its content. For these systems to be effective, it is necessary to optimize as early as the design stages the generation and employment of natural airflow paths inside the building by increasing their speed and improving the distribution of indoor ventilation [69].

To properly address this issue, contemporary research predominantly employs methodologies such as reduced-scale measurements conducted in wind tunnels, CFD simulations, or a synergistic integration of both in a chained analytical framework.

Wind tunnel experiments require the use of scaled models of buildings subjected to controlled airflow conditions and allow researchers to study the influence of wind on natural ventilation and its dependence on building form [78]. The method allows controlled testing of specific design configurations and provides valuable insights through visual representations of airflow patterns. However, key issues associated with

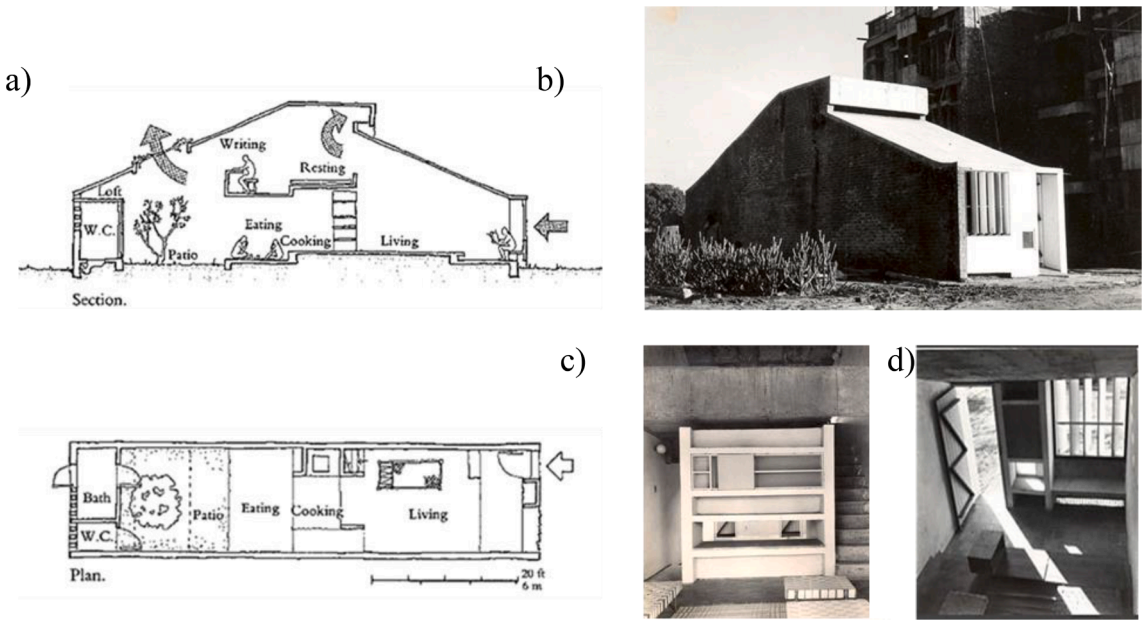

Fig. 2. a) tube house original project; b) prototype external view; c) prototype internal view, d) main façade openings internal view.

the method relate to scaling effects, which can introduce inaccuracies and potentially limit the generalisability of results. In addition, the limited range of environmental conditions turn the assessment of multiple NV scenarios or complex building geometry hardly feasible. Furthermore, the analysis lacks the provision of temperature and thermal comfort data in association with ventilation, focusing solely on the characterization of airflow patterns.

Conversely, CFD is recognized as the most accurate and reliable modelling method to predict natural ventilation in buildings [79]. Indeed, CFD offers a comprehensive understanding of flow patterns and thermal characteristics in the whole building field that are challenging to forecast using alternative methods [80].

As one of the main benefits of CFD applications is the ability to assess and predict the indoor airflow performance of multiple natural ventilation scenarios without the need to gather real monitored data or physical model, especially in the early design stage [81]. Despite its demanding computational requirements and time-consuming nature, this analysis yields a cost-effective approach capable of accommodating complex building geometries and varying environmental conditions facilitating quantitative assessments of airflow dynamics. In addition, CFD simulations allow airflow parameters to be related to thermal comfort assessment as a stand-alone analysis or integrated with building energy software [82].

Along this line, this work, combining computational fluid dynamics (CFD) with building energy modeling (BEM), evaluates the impact of building form and natural ventilation on the thermal comfort of low-income social housing prototype designed by the architect Charles Correa in Ahmedabad, India. The primary research objective is to assess the potential of NV to improve thermal comfort in a hot and arid climate by optimizing building design to alleviate energy poverty in rural areas of the Global South.

2. Case study

With the growing global demand for active cooling, India is poised to become the largest source of cooling-related emissions among the world's leading economies. According to the latest available Census of India survey [83], in 2011, the residential sector in India housed over 18 % of the world's population in more than 250 million homes, yet still had a limited adoption of energy-intensive active cooling technologies.

Over the past few decades, the market share of room air conditioners (RACs) in India has grown significantly, especially in economically thriving and urbanizing cities, thanks to the rapid development of urban infrastructure and a growing economy [5]. The total energy used for cooling in the building sector, which was approximately 126 TWh in 2017, is projected to more than double reaching around 281 TWh by 2027.

While the relative share of cooling energy demand for all sectors will remain more or less the same in 2017 and 2027, space cooling in the buildings sector will continue to dominate, accounting for around 57% of total cooling energy demand in 2027 [84]. Given the significant increase (1.5–2 times) in building area by 2027 compared to 2017 levels, it is important to reinforce the need to incorporate strategies and measures to passively reduce cooling demand itself, ensuring widespread access to affordable thermal comfort.

In an effort to address the same issue, Indian architect Charles Correa set out in the 1960s to improve the thermal comfort and affordability of cooling for low-income people by incorporating specific building designs to meet their climate control needs. During the 1960s and 1970s, India, after gaining independence, lacked the energy capacity necessary to provide optimal indoor climate conditions for its entire population. This realisation prompted the search for alternative methods of creating habitable built environments. This posed a significant challenge to architects, who had to design low-energy buildings that could passively provide thermal comfort within the constraints of affordability and availability of energy resources.

Correa's involvement in a national competition organized by the Department of Public Housing in 1960 led to the inception of the Tube House project. The competition sought innovative concepts for affordable buildings, and the project's emphasis on passive architecture won it the first prize (Fig 2). In this project, the architect aims to enhance the indoor comfort of buildings by maximizing natural ventilation potential through shape optimization. This involves creating pathways and velocities that promote better airflow, ultimately improving the overall perception of comfort for the occupants.

The Tube House takes on a simple parallelepiped shape, with a plan measuring 16.2 by 3.9 m. Its design draws inspiration from the vernacular architecture of northern India, characterized by narrow units sharing side walls. In this configuration, the two longer sides do not receive direct heat input, and all ventilation and natural light enter through the shorter facades. This layout bears a resemblance to a tube, lending the project its name.

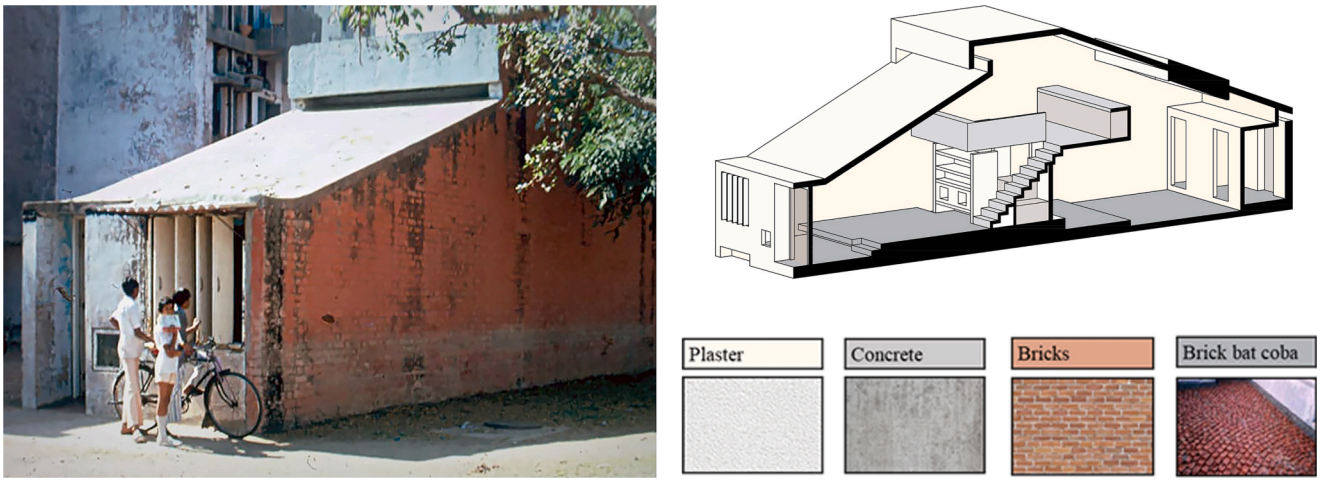

Fig. 3. Tube House materials characterization.

Drawing from this historical architectural heritage, the architect adopts a predominant longitudinal layout for the building. Additionally, two parallel closed baffles are strategically positioned opposite the shorter sides that face the prevailing wind, allowing for effective capture of the wind. To enhance natural ventilation and cooling, the sloped roof incorporates ventilation openings at the upper section and at the back. In the absence of wind, the top inlet acts to expel hot air from the building, drawing in fresh air from below and promoting convection currents that enhance the thermal buoyancy effect; in the presence of wind, it acts as a wind catcher, allowing fresher air to enter from higher up.

The building is designed to accentuate thermal *alliesthesia* [99], which refers to the interdependent relationship between an organism's ever-changing internal state and the pleasure or displeasure experienced by certain stimuli [85]. By optimizing the building's form, the use of natural ventilation, and the modulation of airflow speed within the building, it carefully avoids the uniformity imposed by mechanical ventilation and air-conditioning systems. This intentional variation in environmental conditions creates a sense of "change", effectively combating thermal monotony and aligning with the hedonistic principle that underlies the perception of well-being, thereby stimulating the building's occupants, especially in hot climates.

To meet this challenge, the building's design envisages a seamless environment with no internal divisions or cross-walls to obstruct airflow, linking the windward and leeward sides to optimize cross-ventilation efficiency. This approach results in a versatile spatial continuum where the distinction between the different spaces of the building is based on different horizontal levels. These different heights create a spatial hierarchy that effectively organizes the different living functions within the building.

In the Tube House, a cost-effective approach for material selection was adopted (Fig. 3). Glazed window frames are replaced with all-wood frames, while the openings at the base of the building and in the courtyard are covered with metal grilles to ensure proper ventilation. Brick is used for the side walls and reinforced concrete for the structural elements, internal partitions, staircase and pitched roof. For the ground slab, a traditional Indian construction technique called "brick bat coba" is employed. This technique is well-suited due to its excellent thermo-hygrometric and waterproofing properties. It involves submerging brick fragments in a cement mortar, effectively preventing rising dampness from the ground.

2.1. Site and climate

The Tube House prototype was built in the city of Ahmedabad in western India, in the state of Gujarat. The city belongs to the *Bsh* (sub-tropical steppe climate) climate zone according to the Köppen-Geiger classification and climatic zone 0B according to ASHRAE Standard 169. This zone is characterized by a hot arid climate with very low percentage of annual precipitation. Based on the TMY of the weather data file for Ahmedabad, the city turns out to be a cooling dominated climate with a total of 3460 CCD calculated with a base temperature (T_{base}) of 18 °C as recommended for India by Bhatnagar et al [86] and only 2 HDD. The city experiences cooling demand throughout the year, with the highest values occurring from April to June (Fig. 4).

The region faces three main seasons: summer, monsoon, and winter. Except for the monsoon period, the climate remains notably dry. From March to June, the weather turns very hot, with average summer

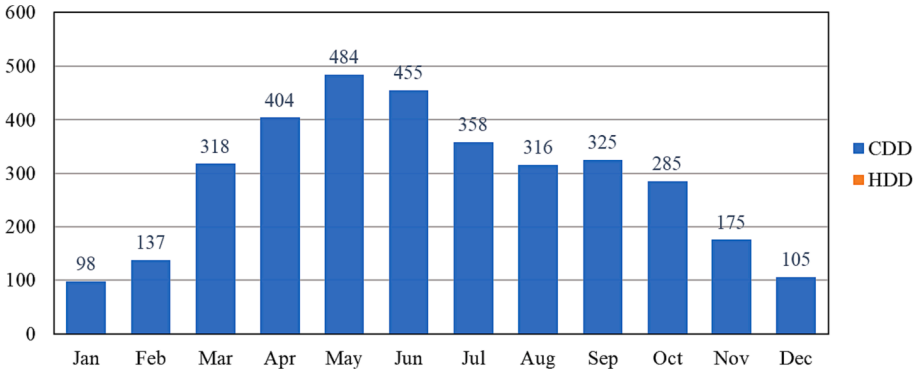

Fig. 4. Cooling and Heating degree days according to ASHRAE for the city of Ahmedabad, India [86].

Table 1
Ahmedabad climatic conditions.

Location	Ahmedabad
Latitude	*23° 01′ 48″ N*
Longitude	*72° 34′ 48″ E*
Prevalent wind	*SW*
Average wind speed	*2.01 m/s*
Köppen climate classification	*Bsh*
Average yearly temperature	27.2 °C
Outdoor T_{max}	*43.9 °C (13th May)*
Outdoor T_{min}	*13 °C (10th March)*
Annual cumulative horizontal solar radiation	*2023 W/m²*

maximum temperatures reaching 43 °C and average minimum temperatures settling around 24 °C. Transitioning to November through February, the average maximum temperature decreases to 30 °C, while the average minimum drops to 13 °C. The southwest monsoon sets in from mid-June to end-September, bringing a humid climate to the area. In May, the highest temperature of the year reaches 43.9 °C, while the lowest temperature, recorded in March, drops to 13 °C. Prevailing winds blow from the SW and N directions. The average annual wind speed stands at 2.0 m per second, with maximum wind speeds exceeding 27.8 m per second. The main characteristics of Ahmedabad's climatic conditions are reported in Table 1.

3. Methodology

In this study, the assessment of cross-ventilation's cooling potential on thermal comfort in Tube House follows a four-step modeling system:

- Step 1: *External Wind-Induced pressure*

Initially, a 3D RANS equation with a k-ω SST turbulence model simulation was performed using Ansys Fluent to evaluate the wind-induced pressures on the building surfaces. This analysis helps to understand the impact of external wind on the building surfaces.

- Step 2: *Wind-Induced Natural Indoor Ventilation*

From the average pressures obtained at the building openings, the behavior of wind-driven natural indoor ventilation was simulated to assess the distribution of indoor airflow and average air velocity within the building. The computational fluid dynamics (CFD) domain used for this analysis is the building envelope itself.

- Step 3: *Thermal Dynamic Analysis*

The indoor airflow characteristics obtained in the previous step were utilized to evaluate the influence of natural ventilation on the building's thermal behavior. A thermal dynamic analysis was performed on an hourly basis using DesignBuilder (DB) for three typical days, representing three seasons identified by the Indian Meteorological Department for Ahmedabad.

- Step 4: *Comparison and Thermal comfort evaluation*

Finally, the operative temperatures for the three typical days were compared with acceptability limits provided by the Indian Model for adaptive comfort. To achieve this, two long-term discomfort indexes were evaluated using Matlab data processing.

Overall, this comprehensive modeling approach allows for an in-depth understanding of the impact of cross-ventilation on thermal comfort in the case study in order to assess the efficiency of NV in achieving indoor comfort while also reducing cooling energy consumption (Fig. 5).

3.1. External CFD model

The CFD simulation encompasses two distinct models, namely the external and internal models. The external model is primarily dedicated to analyse the aerodynamic characteristics of the building's surrounding environment, including both the building itself and the surrounding calculation domain.

During this computational process, the building's air inlet and outlet openings remain in a sealed state, with exclusive attention given to the extraction of pertinent data in the form of pressure coefficients at these orifices. Conversely, the internal model is employed to simulate the internal aerodynamic conditions within the building, with a specific emphasis on the airflow dynamics contained therein. Subsequently, the indoor air velocity and airflow distribution are derived through the incorporation of external model-derived pressure values at the building's openings as boundary conditions.

The initial modeling step involves conducting a CFD analysis to assess the external wind-induced pressures acting on the building surfaces. This analysis is conducted using a 3D RANS equations simulation with Ansys Fluent 2021 R1. The simulation procedure adheres to the guidelines set by a previous study conducted by Perèn et al. [87], who performed a validated CFD analysis for a cross-ventilated building with a similar shape.

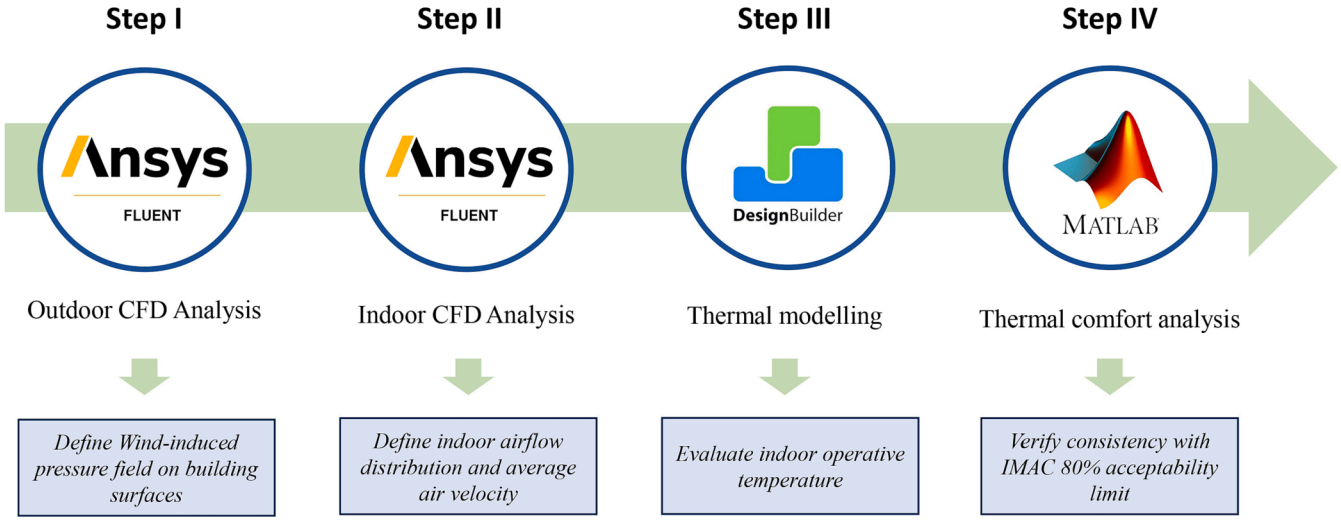

Fig. 5. Software used in this work and timeline logic of their use.

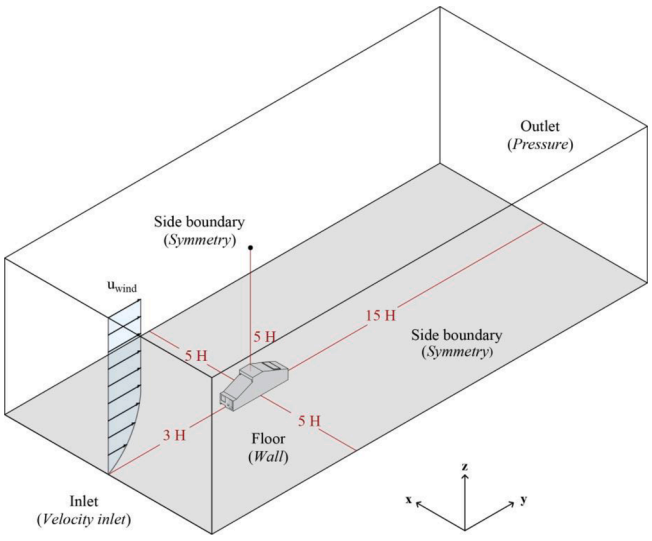

Fig. 6. Computational domain and boundaries conditions.

With the building height (H) as a benchmark, the computational domain size was determined by considering 5H between the side boundaries of the external calculation domain and the building, and 15H between the outlet and the building. To ensure limited horizontal inhomogeneity of the approach-flow profiles [88], the upstream length of the domain was reduced to 3 times the height of the building. For the top boundary, it was positioned 5H above the roof, resulting in a blockage ratio of 1% (less than the recommended 3%). The computational domain is built on a full scale with dimensions of 62 m × 120 m × 35 m for depth, width and height, as shown in Fig. 6.

The extrusion method is used to divide the external mesh, which is a meshing method that extrudes the high-quality surface mesh along a specific path to generate volume mesh. The hexahedron element is adopted, and the boundaries and building openings are locally densified, with a total cell number of about 1,588,576 with a minimum cell size equal to 0.2 m and a maximum one of 0.5 m at the domain edges. The openings of the building were kept closed during the calculation, so as to extract the static pressure data on its surfaces.

At the inlet of the domain, the vertical approach-flow profiles of the mean wind speed u, turbulent kinetic energy k, and specific dissipation rate ω are imposed. The wind direction is perpendicular to the windward building facade. The inlet mean wind velocity profile u(z) is defined according to the logarithmic law (Eq. (1), where u^* is the friction velocity, k *is* the von Karman constant (0.41) and z is the height coordinate.

$$u(z) = \frac{u^*}{k}\left[\ln\left(\frac{z+z_0}{z_0}\right)\right] \tag{1}$$

The value of u^* is determined based on the values of the wind site reference speed (U_{ref} = 2.0 m/s) at reference height (z_{ref} = 10 m). The aerodynamic roughness length is set equal to 0.05 m as for open land. The turbulence dissipation rate ε is calculated using Eq. (2).

$$\varepsilon(z) = \frac{(u^*)^3}{k(z+z_0)} \tag{2}$$

While the specific dissipation rate ω for the SST k-ω model is calculated using Eq. (3):

$$\omega(z) = \frac{\varepsilon(z)}{C_\mu k(z)} \tag{3}$$

where Cμ is an empirical constant taken equal to 0.09.

At the outlet plane, zero static gauge pressure is applied and at the top and lateral sides of the domain zero normal velocities and zero normal gradients of all variables are imposed.

The 3D steady RANS equations were solved in combination with the shear stress transport (SST) k-ω model for the turbulence solving method which is recognized as the most appropriate for the isothermal analysis of natural ventilation in a cross-ventilated building between standard *k*-epsilon, RNG model and Shear–Stress–Transport (*k–ω* SST) turbulence models, by Perèn et al. [89], Ramponi et al. [90], Wang et al. [91] and Mohotti et al [92].

The SST k-ω model applies an automated wall treatment for the ground and building surfaces, which automatically switches between low-Reynolds number modeling and standard wall functions by Launder and Spalding [93] in conjunction with the sand-grain based roughness (kS) modification defined by Cebeci and Bradshaw [94]; depending on the mesh resolution near the wall. The coupled algorithm was used for pressure–velocity coupling, pressure interpolation was second order and second-order discretization schemes were used. Convergence was assumed to be obtained when all the scaled residuals levelled off and reached a minimum of 10^6 for x, y and z momentum and 10^4 for k, ω and continuity.

3.1.1. *External Wind-Induced pressure*

Understanding the three-dimensional wind flow around a building is crucial for comprehending the wind-driven ventilation mechanisms inside it. In Fig. 7, the ambient wind flow pattern around the Tube House is illustrated, revealing three distinct areas: the upward circulation zone (A), the upward separation zone (B), and the leeward recirculation zone (C).

The presence of separation and recirculation zones indicates the

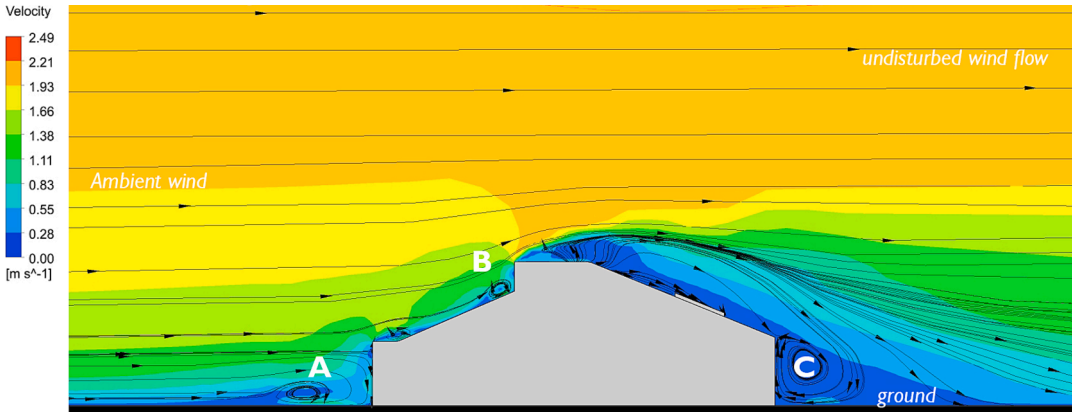

Fig. 7. Wind velocity streamline at the cross-section of Tube House.

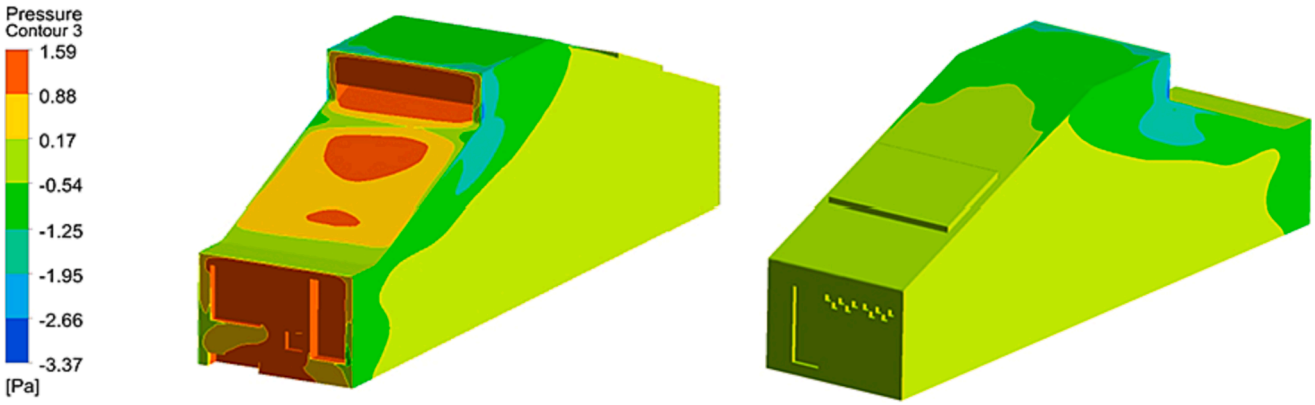

Fig. 8. Three-dimensional distribution of the pressure field induced on the Tube House by the wind.

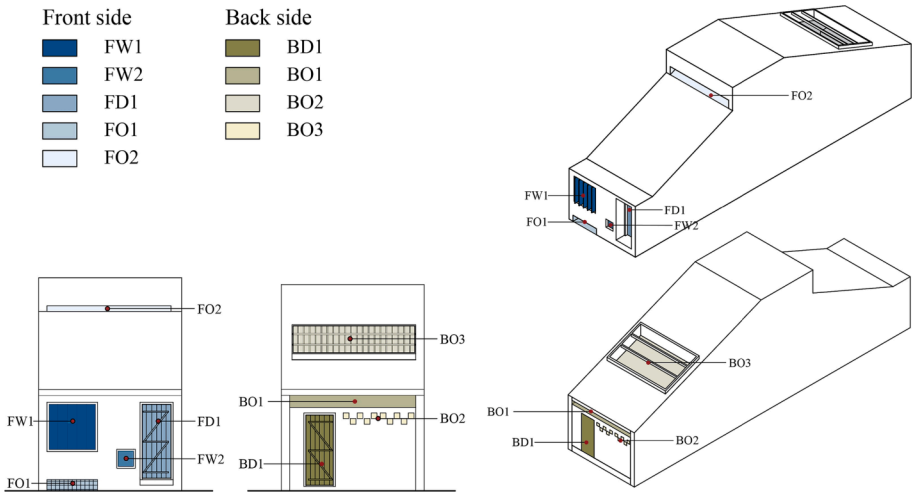

Fig. 9. Tube House openings classification.

complex nature of wind flow around the building and it also suggests that different areas of wind flow may impact the inlets and outlets, leading to significant variations in wind pressure results modifying cross-ventilation efficiency. In line with the log law wind profile, the wind speed experiences a gradual increase from 0 m/s at ground level to 1.78 m/s at the building's top edge.

The collision with the building causes a modification of the components of the initial wind velocity vector, leading to changes in surface pressure as depicted in Fig. 8. Consequently, the atmospheric pressure field surrounding the building is altered, converting the kinetic energy of the airflow into potential energy, resulting in a pressure differential on building surfaces.

This leads to the creation of higher pressure (overpressure) in the upwind zone and lower pressure (depression) in the downwind zone, as well as on the back side of the building. This setup allows a detailed examination of wind pressure variations at various openings throughout the building. On the slope facing the prevailing wind, specifically the SW side, the wind generates positive pressures on the windward facade, with the highest values observed at the edge of the roof, reaching 1.23 Pa.

The front roof pitch experiences partial depression: the first half is depressed with values in the middle at around −0.44 Pa, while the upper part shows overpressure. The upper part of the windward stratum, where the upper opening is located, registers the highest overpressure, with a maximum value at the center of 1.56 Pa. The horizontal top of the stratum and the rear stratum are both in a state of depression, with more significant negative pressure values observed at the edge adjacent to the windward facade (-1.09 Pa).

As one descends towards the downwind side, the negative pressure values gradually decrease. At the edge of the rear façade, pressure values of −0.10 Pa are recorded. The surfaces perpendicular to the wind direction are also experiencing depression, with the most significant negative pressure values recorded near the edge of the roof, reaching a maximum value of −2.65 Pa.

The openings are kept closed during the simulation, and the pressure coefficient of each opening is extracted to calculate the integral mean value as the boundary conditions of the internal model. Each inlet and outlet are numbered as shown in Fig. 9, while Table 2 illustrate the static pressure values induced by prevalent wind speed on building openings.

Results show the static pressure of the openings on the windward side are all positive, while the openings on the leeward side and the top interface are mainly negative. However, perhaps due to the effect of the

Table 2
Static pressure values at the Tube House openings corresponding to prevalent wind speed.

Static pressure [Pa]			
Inlet		*Outlet*	
FW1	1.17 Pa	BD1	−0.07 Pa
FW2	1.10 Pa	BO1	−0.17 Pa
FD1	0.95 Pa	BO2	−0.10 Pa
FO1	1.01 Pa	BO3	−0.27 Pa
FO2	1.32 Pa		

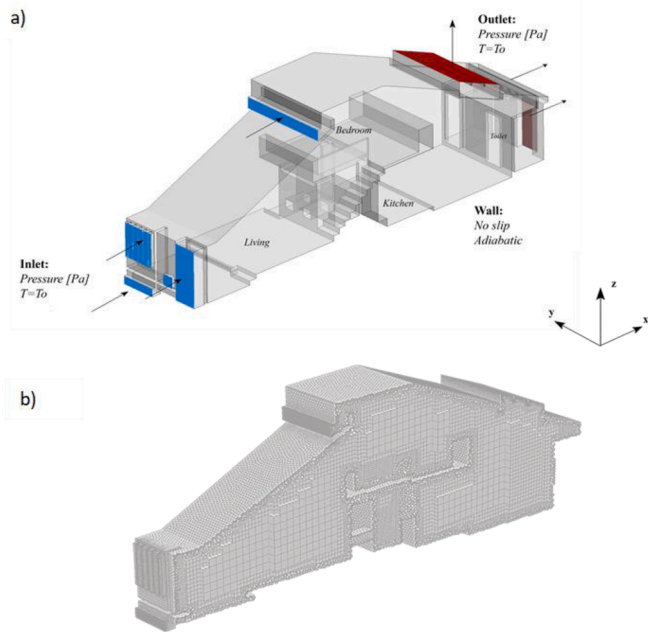

Fig. 10. a)outline of boundary conditions; b) illustration of the final mesh for the fluid domain of the building.

recirculation zone, the lower openings, on the leeward side, reports low depression values.

The strategic placement of the top opening at the back of the leeward roof, where a higher value of depression is observed, emphasizes the variation in wind pressure aiming to promote cross-ventilation within the building.

3.2. Internal CFD model

Openings integral pressure values were set as boundaries conditions of the indoor computational domain. The indoor CFD analysis was performed to evaluate the entity and distribution of air velocities within the building due to wind-driven cross-ventilation corresponding to reference site wind speed. The building's envelope served as the computational domain for the analysis and defined the volume of the fluid domain.

Regarding the boundary conditions for the computational domain, all walls are subjected to a no-slip boundary condition, and an adiabatic boundary condition is applied as well. The inlet and outlet boundary conditions are tailored to align with the building openings (Fig 10a).

For the inlets and outlets, pressure boundary conditions are implemented based on the pressure values obtained from the initial CFD analysis. The windward openings are designated as inlets, following the results from the outdoor CFD analysis, while the leeward openings are treated as outlets. Based on the wind-induced pressure values, the top opening FO2 located at the roof vertex is designated as an inlet, whereas the back opening BO3 is specified as an outlet.

In this simulation, the 3D steady RANS equations were solved along with the shear stress transport (SST) k-ω model. The pressure–velocity coupling utilized a coupled algorithm, employing second-order pressure interpolation and second-order discretization schemes.

3.2.1. Grid sensitivity analysis

The computational domain's grid was generated using polyhedral cells. To determine the number of cells for the computational domain, Eq. (4), which is recommended for indoor environments by Nielsen et al. [79], was used for a preliminary assessment.

$$N_{cell} = 44.4 \bullet 10^3 \bullet V^{0.38} \quad (4)$$

Table 3
Grid independence analysis.

	No. of cells	Average air velocity across the diagonal m/s	Domain average air velocity m/s	Inlet Mass flow m^3/s
M1	164,651	0.148	0.514	3.531
M2	329,303	0.145	0.491	3.857
M3	658,606	0.144	0.485	3.851

To test the grid sensitivity of the internal models and improve the accuracy of the calculation results, three different mesh models are established by using the mesh extrusion method.

As suggested by Chen and Srebic [95], a reliable method for verifying the numerical model is to systematically refine the grid size by doubling the number of grid elements and then comparing the corresponding results. Using the number of cells obtained from Eq. (4) as the medium level, three mesh models were analyzed: a coarse mesh model with 164,651 cells (M1), a medium-mesh model with 329,303 cells (M2), and a fine mesh model with 658,606 cells (M3). To ensure a precise comparison and to evaluate all regions within the domain, three parameters were considered: the mean value of air velocity along the diagonal line connecting two corners of the domain, the average air velocity within the domain, and the inlet mass flow. Table 3 shows the comparison between the three mesh models results.

The results of the coarse mesh model deviate to some extent, while the other two models fit well, which indicates that the medium mesh model already has a certain accuracy and can be selected in the calculation of internal models to save the cost. The variation between the results obtained using the finer mesh (M3) and the medium mesh (M2) is as follows: 1.4% for the average air velocity along the diagonal line, 1.2% for the overall average air velocity, and 0.2% for the inlet mass flow. These small discrepancies indicate that the differences between the two mesh models are negligible, affirming the mesh independence of the results.

Incidentally, the selected final polyhedral mesh for the simulation (Fig 10b) consisted of 898,090 cells and a total of 2,806,885 nodes, makin it nearly 2.7 times finer than the recommended mesh (M2).

A non-uniform grid strategy was used to ensure accurate results. This approach involved using a higher mesh density around the inlets, outlets and solid walls, while using a lower mesh density with an expansion rate for the far field regions. To achieve the desired level of detail in the analysis, a minimum cell size of 0.02 m for the critical regions and a maximum cell size of 0.1 m for the far field regions were chosen. The initial tetrahedral mesh was later converted to a hexahedral mesh to improve grid quality.

Furthermore, since meshes with a high aspect ratio can result in low accuracy and a slow rate of convergence, a maximum aspect ratio value of 8.1 was achieved in mesh generation, in line with recommendations to keep it below 50.

In addition, particular attention was paid to the skewness value, which represents the difference between the shape of the cell and the shape of an equilateral cell of equivalent volume, ideally lying within a range from zero (representing optimal conditions) to one (representing suboptimal conditions). In this research, the skewness parameter has an average value of 0.41 [96].

Finally, to enhance the accuracy of the results near the wall the enhanced wall-treatment has been monitored in wall regions. The near-wall mesh has a $y+ < 1$ value, for the other surfaces, the value of $y+$ is satisfied with $30 < y+ < 300$ as recommended. The accuracy of the current CFD model is verified by comparing the experimental and CFD simulated data obtained from the studies of Karava et al. [97] and Perèn and Blocken [89] in Appendix 1.

Convergence was considered achieved when all the scaled residuals reached a minimum of 10^{-6} for x, y, and z momentum and 10^{-4} for k, ω, and continuity, signifying a leveling off in their values. The results are

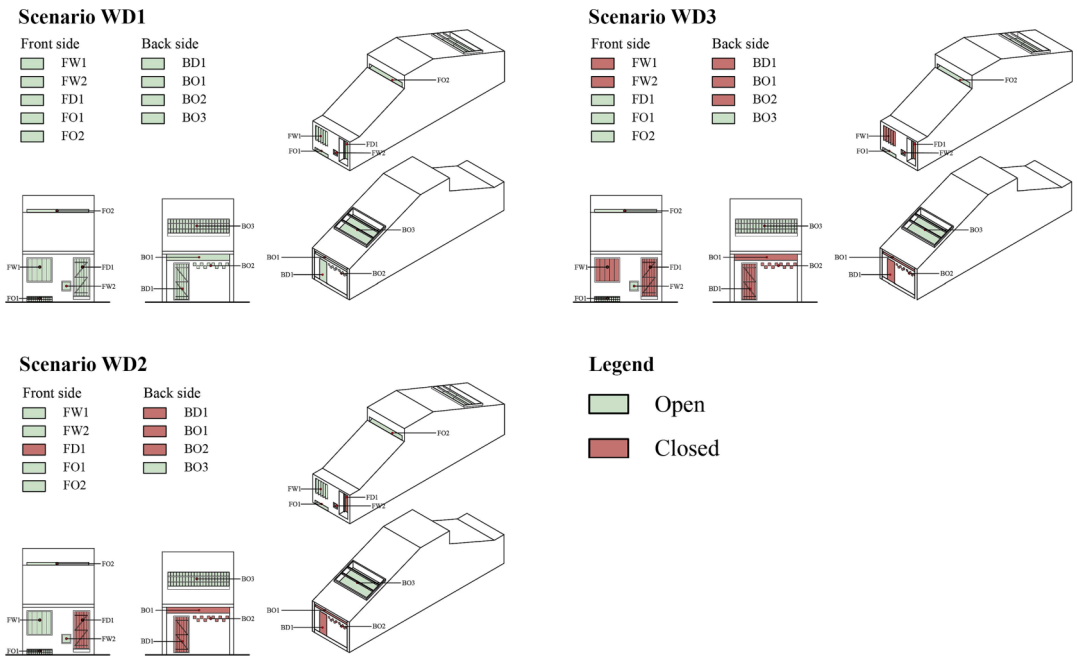

Fig. 11. Schematisation of the operation of the different openings' configurations analyzed in the different scenarios.

monitored over 5,000 iterations and the final values are obtained by averaging over 400 iterations after the simulation has reached a statistically stationary solution, in order to obtain a reliable steady value of the solution variables. After convergence is reached, the error in mass flow balance of the indoor space is less than 10^{-4}.

3.2.2. *Openings configurations*

To consider the various locations and types of openings, three distinct scenarios of opening combinations, involving inlet and outlet openings, were analyzed. The first scenario (WD1) investigates cross-ventilation within the building, considering all openings as active. In the second scenario (WD2), openings that are not strictly necessary or typically kept closed, such as the entrance door and service access rooms, are considered.

The last scenario (WD3) only considers openings that do not have closures and are perpetually open, namely, the ventilation grille at the base of the windward façade, the air intake at the top of the roof pitch, and the skylight at the rear of the building. Fig. 11 illustrates the inlet and outlet combinations considered in each scenario.

3.3. *Thermal model*

To evaluate the impact of cross-ventilation on the thermal performance of the case study, a dynamic thermal simulation was conducted on an hourly basis. This simulation was performed on DesignBuilder® software, where the indoor ventilation outcomes obtained from the CFD analysis were incorporated into the building's thermal mode. The climate file Ahmedabad ISHRAE in the *Energyplus* archive was used as the climate file.

Regarding the simulation's envelope characteristics, the external walls primarily comprise bricks (U-value = 2.32 W/m^{2}K), the roof is composed of non-insulated reinforced concrete (U-value = 2.93 W/m^{2}K), and the ground floor is a composite structure of concrete and non-insulated brick (U-value = 2.79 W/m^{2}K). Additionally, wood shadings were assumed to be used for the windows.

As the free-running behavior of the building was only studied under the effect of natural ventilation, no mechanical systems were used.

The thermal results of three typical days corresponding to the cooling season as identified by the Indian Meteorological Department are extracted. Specifically, May 13th is the hottest day of the year, with a maximum external temperature of 43.9 °C and a minimum of 29.4 °C during the summer period; August 16th with a maximum temperature of 33.2 °C and a minimum of 26.1 °C during the monsoon period; and September 30th, representing the end of the monsoon period, characterized by a maximum temperature of 34.1 °C and a minimum of 25.8 °C. The temperature excursion between day and night on the three analyzed days is equal to 14.5 °C on May 13th, 7.8 °C on August 16th and 8.5 °C on September 30th respectively.

Three distinct simulations were conducted to correspond to various scenarios of openings configurations. The airflow distribution observed in the CFD analysis within the analyzed scenarios was incorporated into the thermal simulations. During this process, all factors such as occupancy, envelope characteristics, internal loads, and operation schedules of the openings remained consistent, except for the natural ventilation features depending on CFD results.

To prevent natural ventilation from overheating the indoor spaces during the hottest hours of the day, based on the site climatic conditions, an operating schedule for the openings was planned that would reduce the percentage of total opening surface depending on the outside temperature. Consequently, during the hottest hours, scenarios WD1 and WD2 were configured with the same ventilation setting as WD3, signifying the more closed configuration available.

To assess the influence of NV on the thermal behaviour of the building the results of three cross-ventilated scenarios were compared with the scenario WD0 which considers the total absence of NV except for minimal ACH (0.3 h^{-1}). Air temperature and mean radiant temperature results by thermal simulations were extracted for each scenario.

3.4. *Thermal comfort assessment*

In the final step, the indoor operative temperatures for each scenario are assessed to determine their compliance with the indoor thermal comfort limits. Air temperature and mean radiant temperature resulted from thermal simulations were combined in MATLAB along with the average air velocity obtained from CFD analysis for each scenario.

To account for the different average air velocities in the ventilation scenarios, the operative temperature was calculated using ASHRAE Standard 55: 2020 [98] as Eq.5:

Table 4
Values of coefficient A as the relative air velocity varies (Source: ASHRAE Standard 55:2020).

v_r	$v_r < 0.2$ m/s	$0.2 < v_r < 0.6$ m/s	$0.6 < v_r < 1.0$ m/s
A	0.5	0.6	0.7

$$t_o = At_a + (1 - A)\bar{t}_r \tag{5}$$

where t_o is the operative temperature, t_a is the average air temperature, t_r is the mean radiant temperature and A is a coefficient whose value be selected as a function of the relative air velocity v_r as in Table 4.

Among the different worldwide formulations of the adaptive model including the adaptive model proposed by ASHRAE-55:2020 and EN Standard 16798:2019 [99,100], an adaptive model modified specifically for the Indian climate called IMAC-R (India model for adaptive comfort - residential) introduced by Rawal et al. [101] based on IMAC model proposed by Manu et al. [102], was used.

The IMAC model is an adaptation of the adaptive model presented in the ANSI/ASHRAE-55 standard but with modifications based on actual data collected from buildings in India. This model takes into account the distinct cultural and climatic context of India, which differs from the assumptions made in the ANSI/ASHRAE model primarily derived from buildings in temperate/cold climates. Through experimental findings, it was observed that the comfort standards of the Indian population have higher limits of perceived comfort compared to the predictions provided by the ANSI/ASHRAE-55 and EN 16798 models. Thus, the IMAC-R proposes an adaptive thermal comfort model based on yearlong field surveys for residential buildings located in eight cities across five climate zones of India, including Ahmedabad.

In contrast to other models, IMAC-R offers the potential to meet the thermal comfort requirements of the Indian population, while also paving the path for sustainable long-term energy savings and climate action. The model prescribes the operative temperature bands for 80% and 90% thermal acceptability in correlation with the outdoor reference temperature, applicable to mixed-mode (MM) and naturally ventilated (NV) buildings.

According to the IMAC-R model, the neutral temperature in naturally ventilated buildings can vary between 19.9 °C and 31.5 °C for a moving average of the T_{out} (30-days outdoor running mean temperatures) between 5.5 °C and 33 °C. The operative temperature consistent with the IMAC-R limits can range between 16.3 °C and 35 °C, resulting warmer than the temperature prescribed by the recent ASHRAE-55 and EN 16798–1 models by 2 °C and 0.3 °C, respectively. Equation (6) presents the mathematical expression provided by the model for calculating the neutral temperature, as well as the upper and lower 80% and 90% acceptability limits.

$$\begin{cases} Upper\ 80\%\ acceptability\ limit\ (^\circ C) \\ \quad = 0.42(T_{out-30DRM}) + 21.20 \\ Upper\ 90\%\ acceptability\ limit\ (^\circ C) \\ \quad = 0.42(T_{out-30DRM}) + 21.20 \\ Neutral\ comfort\ temperature\ (^\circ C) \\ \quad = 0.42(T_{out-30DRM}) + 17.60 \\ Lower\ 90\%\ acceptability\ limit\ (^\circ C) \\ \quad = 0.42(T_{out-30DRM}) + 15.45 \\ Lower\ 80\%\ acceptability\ limit\ (^\circ C) \\ \quad = 0.42(T_{out-30DRM}) + 14.00 \end{cases} \tag{6}$$

For residential buildings, the limit to be evaluated is the 80% acceptability limit as provided by the ANSI/ASHRAE-55 model.

Furthermore, two long-term comfort indexes were assessed to compare various scenarios. These indexes include the POR (Percentage Outside the Range) index, which represents the percentage of hours when the operating temperature falls outside the acceptable range predicted by the adaptive model, and the LPD (Long-term Percentage of Dissatisfied) based on the ALD (ASHRAE Likelihood of Dissatisfied), which measures the extent of deviation of indoor operating temperatures from the optimal level [103,104].

The POR, introduced by ISO 7730 and re-proposed by UNI EN 16798–1, requires calculating the percentage of occupancy hours (h_i) in which the real or simulated indoor operating temperature or PMV are outside a specified comfort range relative to the chosen comfort category as follows:

$$POR = \frac{\sum_{i=1}^{Oh}(wf_i \bullet h_i)}{\sum_{i=1}^{Oh} h_i} \tag{7}$$

where w_f is a weighting factor depending on the chosen comfort range.

When referring to the adaptive model, the comfort interval is expressed in terms of operating temperatures and the index is denoted $POR_{Adaptive}$. Its formulation follows the Eq. (8):

$$POR_{Adaptive} \propto \begin{pmatrix} wf_i = 1 & \Leftarrow \left(T_{op,in} < T_{op,lower\ limit}\right)\ V\ \left(T_{op,in} > T_{op,upper\ limit}\right) \\ wf_i = 0 & \Leftarrow \left(T_{op,lower\ limit} \leq T_{op,in} \leq T_{op,upper\ limit}\right) \end{pmatrix} \tag{8}$$

The LPD aims to assess the probability of an uncomfortable phenomenon occurring under certain indoor conditions, was calculated to evaluate thermal stress phenomena. LPD index is calculated as follows (Eq.9):

$$LPD(LD) = \frac{\sum_{t=1}^{T}\sum_{z=1}^{Z}\left(p_{z,t} \bullet LD_{z,t} \bullet h_t\right)}{\sum_{t=1}^{T}\sum_{z=1}^{Z}\left(p_{z,t} \bullet h_t\right)} \tag{9}$$

where t is the counter for the time step of the calculation period, T is the last progressive time step of the calculation period, z is the counter for the zones of a building, Z is the total number of the zones, $p_{z,t}$ is the zone occupation rate at a certain time step, $LD_{z,t}$ is the Likelihood of dissatisfied inside a certain zone at a certain time step and h_t is the duration of a calculation time step (e.g., one hour). The Likelihood of dissatisfied can be formulated in different ways depending on the reference comfort model. Among those in the literature [105], the ALD index (ASHRAE Likehood of Dissatisfied) was used, which is defined in Eq. (10):

$$ALD(\Delta T_{op}) = PPD(\Delta T_{op}) = \frac{e^{-3.057+0.419\Delta T_{op}+0.007\Delta T_{op}^2}}{1 + e^{-3.057+0.419\Delta T_{op}+0.007\Delta T_{op}^2}} \tag{10}$$

where ΔT_{op} is the difference between the indoor operative temperature and the optimal temperature according to the adaptive comfort model. During the analysis, the IMAC-R model's upper and lower limits of 80 % acceptability were employed as threshold values in the computation of the indexes.

4. Results and discussion

4.1. Wind-Induced natural ventilation

After assessing the pressure field induced by the wind on the building's openings, it was possible to analyze the influence of wind-driven cross-ventilation within the building. Fig. 12 illustrates the results of the distribution of airflow velocity induced by wind-driven cross-ventilation as a function of the three different ventilation scenarios.

Evidently, the spatial layout of indoor spaces optimizes the airflow pattern within the building, facilitating a cross-ventilation effect that allows the airflow to cross the building from the windward side to the leeward side, thereby enhancing ventilation.

The spatial continuum inside the building prevents the creation of physical resistance to airflow patterns allowing proper indoor ventilation. The presence of openings on both the windward and leeward roof sides enables the external fresh air to flow along the roof cooling it down. As the total surface area of the opening inlets decreases, the air distribution effectiveness of the building drops despite increasing air velocity.

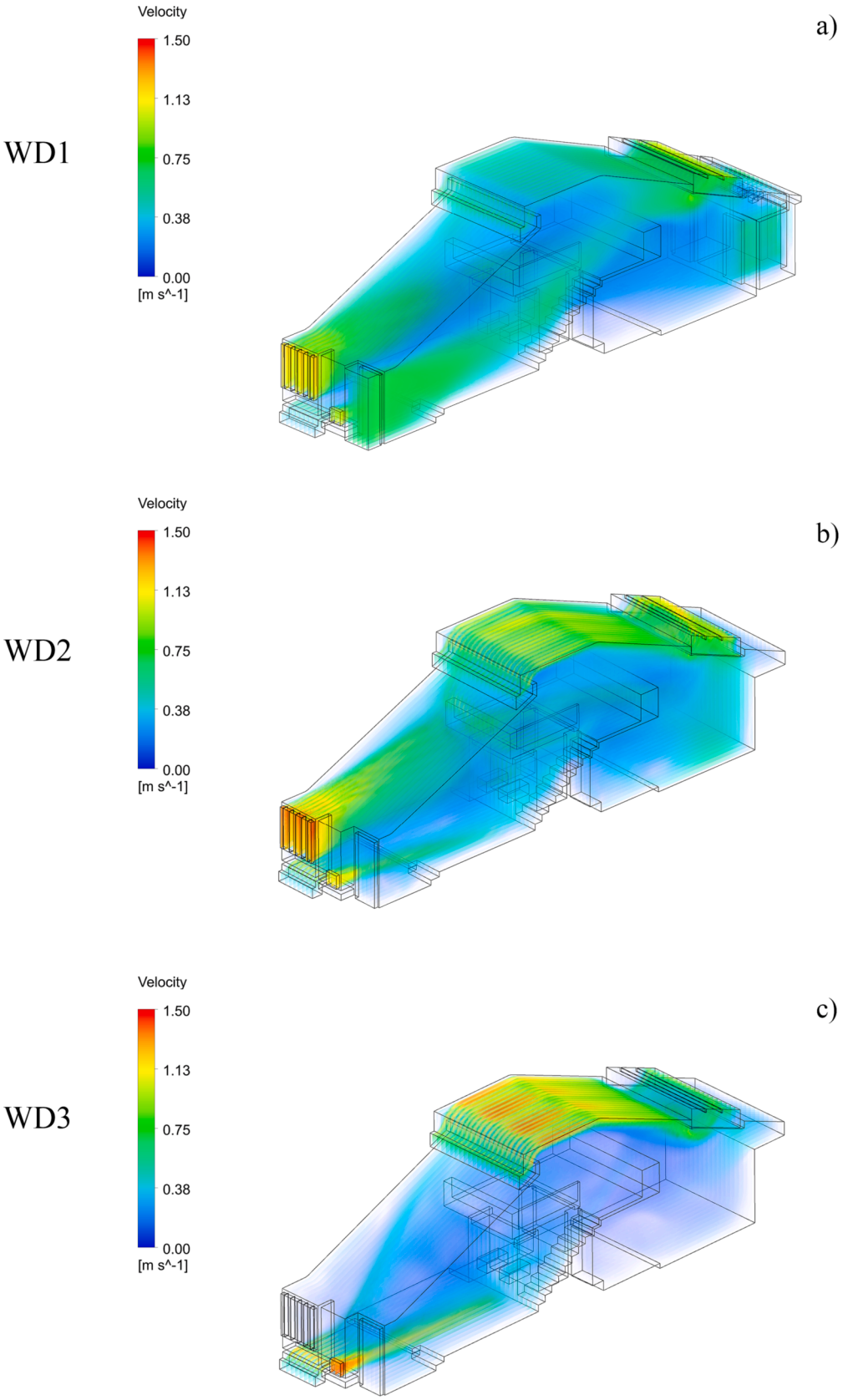

Fig. 12. 3D air velocity distribution for each openings scenario: a) WD1, b) WD2, and c) WD3.

Table 5
Airflow properties for the analysed ventilation scenarios.

Scenario	A_{in}/A_{out} Ratio	Average Airspeed	Max air speed	Air flow rate
	$R_{in/out}$ [-]	u_{ave} [m/s]	u_{max} [m/s]	q_v [m^3/s]
WD1	0.67	0.58	1.24	3.85
WD2	0.50	0.52	1.44	2.77
WD3	0.33	0.26	1.46	1.24

Based on the analysis of scenario WD1 (Fig. 12a), the wind flow enters the building through openings on the upwind façade and on the windward inlet at the top of the roof. Upon meeting the horizontal floor that divides the two levels, the flow splits into two separate currents. One is an upper current which involves the bedroom area, while the other is a lower current passing through the living area. These currents pass through the entire building and exit through openings on the leeward façade and the patio grille on the leeward back roof opening.

In scenario WD2 (Fig. 12b), air velocity values increase compared to WD1 one. This is a result of the decrease in inlet opening surfaces, which creates an acceleration of the airflow near the opening. The airflow concentrates the air current primarily on the East side of the building. By reducing the opening area of the building (WD3) an increase in incoming airflow through the inlet at the rooftop is recorded.

Air enters the building with higher velocity through the ventilation grille located at the lower part of the main façade and the air inlet at the rooftop and exits through the patio skylight. However, the airflow through the building is less intense and less distributed, mainly concentred in the upper part of the building. This current interacts with inclined roof surfaces that receive more solar radiation due to their geometric shape. This interaction increases convective heat exchange, resulting in the cooling of these surfaces. Table 5 reports the CFD airflow properties for the analyzed ventilation scenarios.

Specifically, from each scenario the following parameters are analyzed: the average air velocity in the dwelling (u_{ave}), the maximum air velocity (u_{max}), the ratio between the net area of inlet and outlet openings ($R_{in/out}$), the airflow rate (q_v).

Scenario WD1 exhibits the highest average air velocity in the domain, measuring 0.58 m/s. As the opening surface area decreases, the average air velocity decreases as well, reaching 0.52 m/s in scenario WD2 and 0.26 m/s in scenario WD3. However, interestingly, a reduction in opening surfaces leads to an increase in maximum air velocity, rising from 1.24 m/s in WD1 to 1.46 m/s in WD2, which happens to be the highest value among all the analyzed scenarios.

Wind-driven cross-ventilation, combined with the shape of the building, results in an increasing air flow rate as the surface area of the inlet openings grows, amounting to 1.24 m^3/s, 2.77 m^3/s and 3.85 m^3/s for scenarios WD3, WD2 and WD1, respectively. As a result, scenario

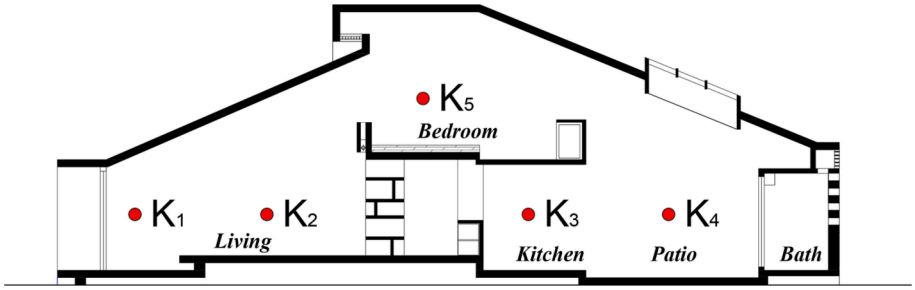

Fig. 13. Schematisation of measuring points (K_i).

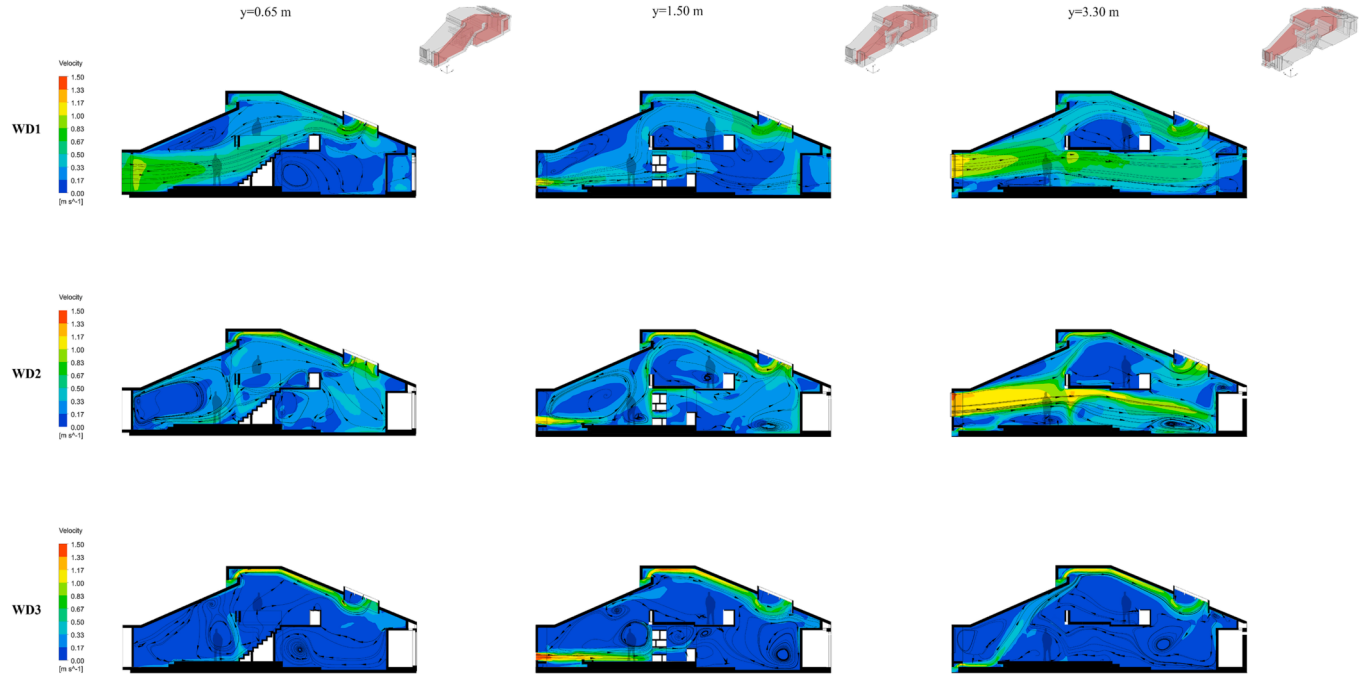

Fig. 14. Comparison of air velocity and velocity streamlines on longitudinal-section in Tube House at different depths (y = 0.65 m, =1.5 m and y = 3.30 m) under different ventilation scenarios.

Table 6
Air velocity values (u) at measuring points (K_i).

Scenario	K_1	K_2	K_3	K_4	K_5
	[m/s]	[m/s]	[m/s]	[m/s]	[m/s]
y = 0.65 m					
WD1	0.80	0.76	0.06	0.20	0.35
WD2	0.06	0.13	0.18	0.37	0.32
WD3	0.08	0.08	0.01	0.05	0.09
y = 1.50 m					
WD1	0.10	0.56	0.15	0.18	0.21
WD2	0.13	0.22	0.27	0.26	0.16
WD3	0.11	0.05	0.04	0.06	0.12
y = 3.30 m					
WD1	0.95	0.65	0.53	0.37	0.10
WD2	1.08	0.66	0.58	0.93	0.05
WD3	0.04	0.09	0.26	0.10	0.09

WD1 achieved the highest ACH value, amounting to 71 h^{-1}, while scenario WD2 reaches an ACH value of 51 h^{-1} and WD3 equal to 23 h^{-1}.

The indoor airflow within the building is influenced by a combination of the various inlet and outlet openings configurations, as well as by the shape of the building. These factors create distinct airflow paths in three sectors, leading to modifications in the distribution of airflow along the longitudinal sections at y = 0.65 m, y = 1.5 m, and y = 3.30 m (Fig. 14).

Several measurement points in the building were used to assess the value of air velocity (u_k) and compared the several scenarios. These points include K1, located at the entrance to the building at half height above ground level, K2 in the living area, K3 in the dining zone just after the kitchen block, K4 positioned in the middle of the patio, and K5, which evaluates air velocity values on the upper floor in the bedroom area at human height (Fig. 13).

In the first section (y = 0.65 m) across the main entrance (FD1) and staircases, scenario WD1 produces the highest airflow through the section, with an average air velocity of 0.40 m/s. As the opening areas decrease in scenarios WD2 and WD3, the airflow path decreases (0.34 m/s and 0.22 m/s), while an increased intensity of airflow is recorded over the roof openings FO1 and BO3.

Table 6 shows the air velocity value achieved by each scenario at the measurement points for the three different longitudinal sections.

In the first section (y = 0.65 m) crossing the main entrance (FD1) and the stairways, scenario WD1 produces the highest airflow through the section measuring an average air velocity of 0.40 m/s. As the opening surfaces decrease with scenarios WD2 and WD3, the airflow path decreases (0.34 m/s and 0.22 m/s), while an increased intensity of airflow across the roof openings FO1 and BO3 is recorded.

In scenario WD1, the airflow primarily enters through FD1 and flows towards the upper part of the building, eventually exiting through the opening on the leeward roof. As a result, scenario WD1 achieves the maximum u-values at points K1, and K2 in the initial part of the dwelling and in the upper zone (K5), while greater air velocity in the back side is reached by scenario WD2 at point K3 e K4. In the y = 1.50 m section, the behavior of the openings in the central cross wall, which separates the living area from the dining area, is highlighted by allowing air to pass between the front and rear of the house. In this case, scenario WD2 measures the maximum values of average velocity equal to 0.37 m/s. By reducing the size of the opening area, the inlet air velocity at opening FW2 experiences a notable increase and reaches the highest recorded value in the WD3 scenario. Scenario WD1 achieves the highest values at points K2 and K5 due to the airflow from the other sections, while scenario WD2 achieves the highest values at the other points.

In the last section (y = 3.30 m), scenario WD2 yields the maximum average air velocity value as well as the highest velocity values at each measuring points expected for K5, where the highest value is achieved by scenario WD1. The section at y = 3.30 m even results in the higher value obtained with the FW1 opening, where the presence of the vertical louvers, by reducing the useful section of the opening, causes a strong increase in the inlet velocities. Although Scenario WD2 achieves a higher inlet air velocity at inlet FW1 compared to Scenario WD1, WD1 provides the most effective airflow distribution across the section, although it is less intense. Scenario WD3 produces an increase in air velocity at inlets FO1 and FO2, creating a more intense flow along the roof surfaces.

4.2. Thermal performance results

Natural ventilation characteristics achieved by the different ventilation scenarios in the CFD analysis were implemented in the thermal model to assess the thermal dynamic behavior of the building under the cross-ventilation effect. Thermal results obtained from scenarios WD1, WD2 and WD3 were compared with the building's thermal performance when no natural ventilation (WD0) was employed, except for the minimum ACH for indoor air quality, set at 0.3 h^{-1}.

Fig. 15 shows the comparison in operative temperature values reached by the different ventilation scenarios compared to the one with no ventilation on three characteristic days: May 13th (the hottest day in Ahmedabad), as well as two typical cooling season days: one falling amid the summer period on August 16th and another towards the end on September 30th.

Thanks to ventilative cooling potential, NV manages to reduce indoor operative temperatures significantly. Compared to the scenario without cross-ventilation (WD0), all the scenarios with natural ventilation, especially at nighttime, provide a reduction in indoor operative temperatures that improves with increasing air change rate and increasing average air velocity. As a result, scenario WD1 exhibits the most effective cooling action, whereas WD3 demonstrates the least, with the ventilative cooling effect of scenario WD2 falling in between.

Focusing on the hottest day analysis (Fig. 15a), when the outdoor temperatures range from 43.9 °C and 29.4 °C, the effect of natural ventilation is clearly shown despite elevated outdoor temperatures. The ventilated scenarios show the most significant reduction in operative temperature during the nighttime, specifically from 20:00 to 9:00 when outdoor temperatures begin to drop. The cooling effect of natural ventilation (NV) is enhanced as the ACH increases, with the most remarkable outcomes observed in scenarios WD1, WD2, and WD3, respectively. The maximum operating temperature difference compared to WD0 is obtained in the WD3 scenario with 3.1 °C reached at midnight. Scenario WD2 reduces the operative temperature by up to 2.6 °C, while scenario WD3 lowers it by up to 2.0 °C.

As outdoor temperatures begin to rise, the naturally ventilated scenarios, despite having the same ventilation as WD3, experience overheating issues compared to the non-ventilated scenario (WD0) due to the inability to fully close the openings. Moreover, this effect can be attributed to the low thermal inertia of the envelope, which prevents it from taking advantage of the nighttime structural ventilative cooling provided by NV.

During the other two typical summer days, when outdoor temperatures are lower and reach a maximum of 34 °C, the beneficial impact of NV on the thermal performance of the buildings becomes more pronounced. Throughout August 16th (Fig. 15b), all naturally ventilated scenarios present a consistent decrease in operative temperature over the course of the entire day. Scenario WD1 accomplishes at 23:00 the maximum temperature reduction of 3.6 °C, scenario WD2 of 3.3 °C and scenario WD0 of 2.7 °C when compared to WD0. At the hottest hour (18:00), scenario WD1 drops the operative temperature by 2.0 °C compared to no ventilated scenario.

On September 30th (Fig. 15c), when the building is less affected by the heat accumulated in the previous day due to lower outdoor temperatures during the night, NV manages to produce the highest operative temperature reduction. A maximum drop equal to 3.9 °C, 3.6 °C and 2.9 °C is achieved by scenarios WD1, WD2 and WD3, respectively. Compared to August 16th, NV improves its effect even during the hottest daytime hours. At peak hour, scenario WD1 produces a decrease in

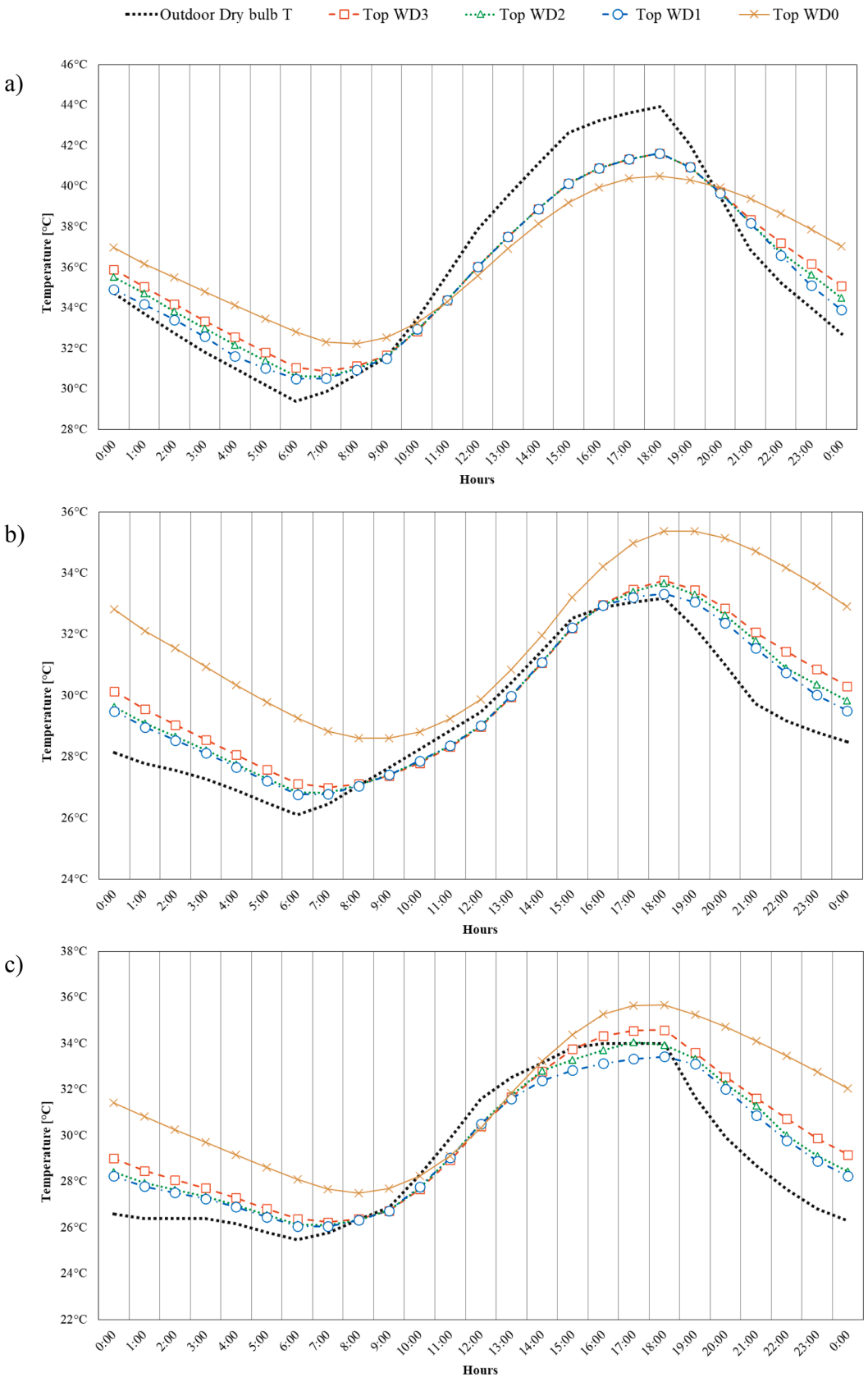

Fig. 15. Operative temperature trend on an hourly basis on a) May 13th, b) August 16th and c) September 30th for the different ventilation scenarios.

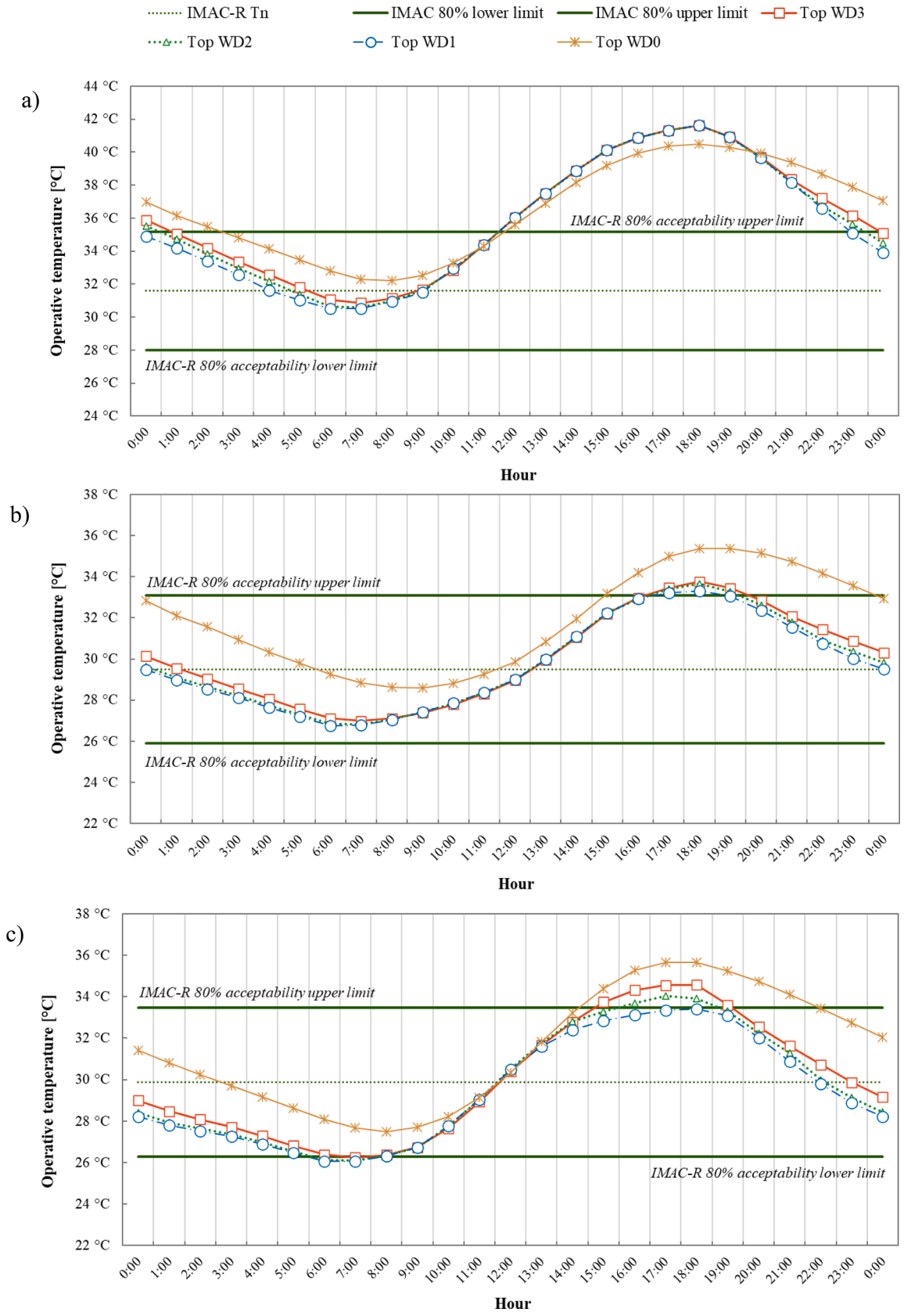

Fig 16. Thermal comfort assessment on a) May 13th, b) August 16th and c) September 30th according to the IMAC-R model acceptability limits.

Table 7
POR and LPD index values on different days calculated for the different ventilation scenarios as ACH increases.

	WD0	*WD3*	*WD2*	*WD1*
$POR_{Adaptive}$ (IMAC-R 80 %)				
May 13th	64 %	52 %	52 %	44 %
August 16th	36 %	12 %	12 %	8 %
September 30th	28 %	24 %	12 %	8 %
$LPD^{<ALD>}_{Adaptive}$				
May 13th	36%	34%	33%	32%
August 16th	17%	11%	11%	10%
September 30th	16%	14%	13%	13%

operative temperature equal to 2.3 °C compared to scenario WD0.

4.3. Thermal comfort results

Fig. 16 reports the operative temperature values achieved by the different scenarios compared to the acceptability limits provided by the IMAC-R comfort model for May 13th, August 16th and September 30th respectively.

The 30-day moving average of the outside temperatures ($T_{out\text{-}30DRM}$) accounted for the three analyzed days is 33.3 °C for May 13th, 28.3 °C for August 16th and 29.2 °C for September 30th.

On the hottest day, operative temperatures exceeding the upper acceptability limit of the IMAC model are observed between 12:00 and 2:00 in scenario without natural ventilation. As the ACH increase, operative temperatures outside the acceptable range start to decrease, reaching lower values with scenario WD1 (from 13:00 to 22:00). Conversely, enhanced ventilation causes operative temperatures to surpass those of non-ventilated scenario during the hottest hours of the day. On August 16th, ventilated scenarios, in contrast with the WD0 scenario, meet the indoor comfort acceptability values for almost the day. The upper limit is surpassed between 17:00 and 19:00 in scenarios WD3 and WD2, while scenario WD1 only reports exceeding operative temperatures from 17:00 to 18:00 when the peaks in outdoor temperature are reached.

In the absence of a cooling natural ventilation effect, scenario WD0 fails to dissipate the overheating during the hottest hours, resulting in a significantly wider range of operative temperatures exceeding the acceptable limits from 17:00 to 23:00.

When analyzing the end cooling period day (September 30th), considering the upper limit of acceptability, scenario WD1 consistently reports acceptable values throughout the day, except for a brief overcooling tendency leading to a temporary surpass of the lower acceptability limit between 6:00 am to 7:00 am. With reduced ACH, the other scenarios experience a lesser overcooling issue compared to WD1. However, they encounter overheating problems during the hottest hours: scenario WD3 from 16:00 to 18:00, and scenario WD2 from 15:00 to 19:00. Moreover, the WD3 scenario extends this period from 15:00 to 19:00.

In contrast, the non-ventilated scenario WD0 exhibits the widest upper limit exceeding period from 15:00 to 21:00 but does not present an overcooling issue consistent with lower acceptability limit.

To evaluate and compare the effectiveness of cross-ventilation's ventilative cooling under various air change rates, a long-term discomfort analysis was conducted, assessing the two indexes POR and LPD, as detailed in Section 3.4. Table 7 shows the POR index values on the typical days for the different simulated ventilation scenarios. On the hottest day, the WD0 scenario reports a POR-value of 64 % in discomfort hours. As the natural ventilation is activated and increased, the POR-value begins to drop, scenarios WD3 and WD2 record 52 % of discomfort hours, while scenario WD1 accounts for a POR-value equal to 44 %, achieving a percentage reduction of 31.3 % in discomfort hours compared to no ventilation scenario.

On August 16th, the POR index is 36 % in the WD0 scenario, 12 % in both WD3 and WD2 scenarios, while it drops to 8 % in WD3, demonstrating how ventilative cooling manages to generate a 77.8 % reduction in discomfort hours inside the building thanks to cross-ventilation during the typical summer day. Similar outcomes are observed on September 30th, with POR-values of 28 %, 24 %, 12 %, and 8 % in scenarios WD0, WD3, WD2, and WD1, respectively.

Scenario WD3 shows a percentage reduction of discomfort hours, compared to WD0, equal to 14.3 %. Meanwhile, scenario WD2 demonstrates a reduction of 57.1 %, and scenario WD1 achieves the least number of discomfort hours, with a reduction of 71.4 % compared to the no ventilation scenario.

Concerning the $LPD_{Adaptive}$ values achieved by the three scenarios on the evaluated days, as the air exchange rate and average air velocity increase, the potential of ventilation cooling to improve thermal comfort conditions increases.

Among the various scenarios, scenario WD1 yields the highest reduction in the probability of dissatisfaction, reaching 11 %, 38.7 %, and 21.5 % when compared to the non-ventilated scenario on the hottest day, August 16th, and September 30th, respectively.

Additionally, scenario WD1 records values closest to thermal neutrality on these specific days, recording the closest values to thermal neutrality among the different scenarios. As the outdoor temperatures decrease, the NV effect in moving towards thermal neutrality improves reducing the probability of an uncomfortable phenomenon.

On typical summer days, during the hottest hours, most ventilated scenarios show ALD values closest to the neutral temperature, promoting a more comfortable environment. However, during nighttime, these scenarios experience higher ALD values than the non-ventilated scenario, as the cooling effect of natural ventilation becomes more pronounced.

Indeed, scenario WD1 shows a higher ALD value on an hourly basis than the one achieved by scenario WD2 because, although it represents the solution with values closer to thermal neutrality during the hottest hours, increasing ventilation flow rates at night when outside temperatures are lower, produces a greater downward deviation of operating temperature from thermal neutrality than values obtained from WD2 scenario, which is characterized by a lower number of changes per hour.

On the hottest day, the non-ventilated scenario exhibits ALD values closer to thermal neutrality during the hottest hours, emphasizing the importance of correctly operating the openings to fully benefit from the potential of natural ventilation. Indeed, during the nighttime hours when the cooling potential of natural ventilation is at its highest, scenarios with increased ventilation result in improved comfort conditions.

4.4. Energy cost impact

The final analysis considers the impact of energy costs and NV energy savings potential on the economic affordability of low-income households. The Government of India's Ministry of Housing & Urban Poverty Alleviation identifies low-income housing (LiH) as housing occupied by households with an annual income between INR 300,000 (USD 3603.5) and INR 600,000 (USD 7207) [106]. Three income bands were evaluated in the analysis: the low band characterised by a monthly income of INR 25,000, the middle band of INR 37,500 and the high band of INR 50,000.

The use of air conditioning (AC) provided by a Room Air Conditioner (RAC) featuring an Energy Efficiency Ratio (EER) of 3, and a mixed-mode scenario (MM) which accounts for the synergistic effect of both AC and natural ventilation were simulated for the three months following the previous analysis: May with 484 CDD, August (316 CDD) and September (325 CDD). To evaluate the indoor comfort threshold and operational mode suitability for the distinct ventilation scenarios, their alignment with IMAC criteria were examined. Specifically, IMAC limits for air-conditioned buildings (IMAC-AC) and mixed-mode environments (IMAC-MM) are used as Ref [102].

Table 8
Incidence of cooling energy costs on the salary of low-income households for different ventilation scenarios.

	CDD	Energy Demand (ED)	Energy Cost (EC)	EC % Impact on LiH Salary		
				Low band	Mid. band	High band
			Air conditioning (AC)			
	°C	kWh	INR	%	%	%
May	484	1,099.5	7,113.8	**28.5 %**	**19.0 %**	**14.2 %**
August	316	428.7	2,773.7	**11.1 %**	7.4 %	5.5 %
September	325	595.3	3,849.7	**15.4 %**	**10.3 %**	*7.7 %*
			Mixed Mode Ventilation (MM)			
	°C	kWh	INR	%	%	%
May	484	560.1	3,623.8	**14.5 %**	*9.7 %*	7.2 %
August	316	173.5	1,122.5	4.5 %	3.0 %	2.2 %
September	325	309.2	2,000.5	*8.0 %*	5.3 %	4.0 %

In "bold" values exceeding the 10 % indicator for energy poverty (EP), in "italic" values with high risk of energy poverty when adding other energy services.
Note: Electricity cost: 6.47 INR/kWh for residential used.

Table 8 illustrates the percentage incidence of cooling energy cost on LiH salary. In all the three analysed months, the cooling energy cost provided by AC alone exceeds the 10 % indicator for energy poverty (EP) [107] for lower LiH band reaching up to 28.5 % of monthly income. For the middle LiH band, exceedances are reported in two out of three months, with the maximum being reached in the hottest month, corresponding to 19 % of monthly income. Even the high LiH band experiences energy poverty in the hottest month. Due to the implementation of natural ventilation (NV) within the mixed-mode scenario, substantial reductions in cooling energy consumption can be achieved, amounting to 49.1 % in May, 59.5 % in August, and 48.0 % in September. NV effectively addresses energy poverty by reducing the 10 % indicator values across all months and income brackets, expect during the hottest month for the lowest band, wherein a remarkable reduction of nearly 50 % in energy cost incidence was achieved compared to AC scenario.

Given that the monthly salary above the PL (poverty line) for rural households in India stands at INR 2,250, both AC and MM result economically unaffordable, leaving NV as the only affordable cooling strategy for approximately 14.6 % of India's population [108].

5. Conclusions

This work, combining building energy modeling (BEM) and computational fluid dynamics (CFD), evaluated the impact of building form and natural ventilation on the thermal comfort of a low-income social housing prototype designed by the architect Charles Correa in India. The analysis demonstrated how proper building form can improve the ventilative cooling efficiency of buildings ensuring indoor thermal conditions even in challenging climatic conditions. Key factors such as sizing and positioning of openings, spatial continuum within the building, as well as the correct operating mode of opening according to external climatic conditions, are found to be crucial to fully benefit from the potential of wind-driven cross-ventilation in buildings.

Results show how the strategic placement of openings relative to wind-induced pressures is essential for enhancing cross-ventilation within the building. Optimal positioning, such as placing openings in the center of the windward facade and the upper part of the leeward side, creates the maximum pressure difference, effectively enhancing the cross-ventilation effect inside the building. Furthermore, reducing inlet openings' surface increases air velocity within the building while negatively affecting airflow distribution across the longitudinal sections.

The proper operation mode of openings is needed to effectively harness the potential of natural ventilation. As, indeed, outdoor temperatures begin to rise, scenarios relying on natural ventilation experienced overheating issues compared to the non-ventilated scenario. This was primarily due to the hot air intake resulting from the inability to fully close the openings.

Although air conditioning proves crucial during the peak hours of the hottest days to ensure indoor thermal comfort and alleviate heat stress, natural ventilation still yields significant benefits in reducing active energy demand, addressing energy poverty. Due to the implementation of natural ventilation within the mixed-mode scenario, substantial reductions in cooling energy consumption can be achieved, amounting to 49.1 % in May, 59.5 % in August, and 48.0 % in September.

Based on the analysis, it was found that scenarios with higher air change rates, achieved through cross-ventilation, offer better thermal comfort conditions inside the building, particularly during periods characterized by a lack of temperature peaks and heavy heat stress.

Even in extremely hot and arid climates, thanks to natural ventilation a maximum reduction in operative temperature of up to 3.1 °C and 3.9 °C is achieved on the hottest day and on the typical cooling period day, respectively. Even discomfort hours drastically drop thanks to natural ventilation cooling potential. As air change rate increases, according to IMAC-R a reduction in discomfort hours up to 31.3 % and 77.8 % on the hottest and typical summer day, respectively, is recorded.

This study emphasized the significance of natural ventilation in addressing energy poverty in rural areas of the Global South, where energy access is constrained, as an efficient technique to provide cooling energy cost savings as well as ensuring comfortable built environments. Future work will include the analysis of natural ventilation driven by thermal buoyancy to assess the potential of natural ventilation depending on the building form, even in the absence of wind. In addition, investigations using future weather data and under different climatic conditions will assess the effectiveness of natural ventilation in coping with energy poverty according to climate changes caused by global warming.

Declaration of competing interest

The authors declare that they have no known competing financial interests or personal relationships that could have appeared to influence the work reported in this paper.

Data availability

Data will be made available on request.

Appendix 1

CFD validation study

To determine the accuracy and reliability of the results of CFD simulations based on the 3D steady RANS equations, model calibration and validation is needed. To validate the CFD process performed in this study, the methodology proposed and used by Pèren et al. [87,89], Ramponi et al.[90], Karimimoshaver et al. [96], Nasrollahi et al. [109] was followed. Specifically, the accuracy of the current CFD model is demonstrated by comparing to the reduced-scale measurements and CFD simulation (SST k-ω) data obtained from the studies of Karava et al. [110] and Pèren et al. [89]. Karava et al. conducted reduced-scale Particle Image Velocimetry (PIV) wind-tunnel experiments to investigate the phenomenon of wind-induced cross-ventilation in a generic isolated building geometry. This study was employed by Pèren et al. to validate the CFD simulation of a building with geometry akin to the present research. The ratio of the computational domain in CFD modellin of the present study aligns consistently with the results of these two referenced studies. The validation study is conducted following the guidelines in Ref. 89.

A quantitative comparison between the measured, computed and the

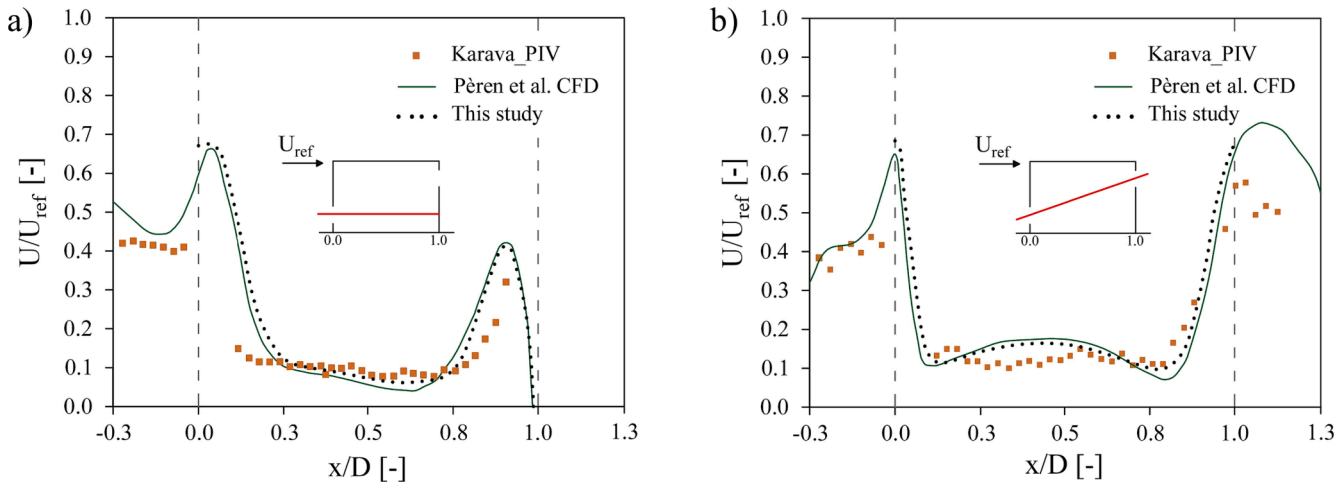

Fig. 17. Comparison of streamwise wind speed ratio U/Uref between PIV measurements by Karava et al. [110], CFD simulation by Pèren et al. [89] and present CFD simulation along: (a) horizontal line and (b) diagonal line of test building.

current study streamwise wind speed ratios U/Uref values are provided along a horizontal line at the midpoint of the windward opening (Fig. 17a) and along a diagonal line between the two opposite openings (Fig. 17b).

The comparison reveals a strong concordance between the measured and computed data and the outcomes derived from the present CFD simulation. A slight difference between the current study results and the referenced ones was observed when comparing the data. Along a horizontal line the simulations give slightly higher values compared to the two cases up to $x/D = 0.3$. Between $0.3 < x/D < 0.8$, the results drop between the two cases to align with the CFD simulation results for x/D values higher than 0.8. This trend also occurs along the diagonal line. Slightly higher values are recorded at the opposite openings, while inside the room the current CFD results agree well with the referenced data. Therefore, the validations show a reliable trend, although some deviations are in line with the results of other research.

References

[1] J. Hansen, R. Ruedy, M. Sato, K. Lo, World of Change: Global Temperatures, Rev. Geophys. 48 (2020), https://doi.org/10.1029/2010RG000345/ABSTRACT.

[2] J. Wang, Y. Guan, L. Wu, X. Guan, W. Cai, J. Huang, W. Dong, B. Zhang, Changing Lengths of the Four Seasons by Global Warming, e2020GL091753, Geophys. Res. Lett. 48 (2021), https://doi.org/10.1029/2020GL091753.

[3] A. Dimitrova, V. Ingole, X. Basagaña, O. Ranzani, C. Milà, J. Ballester, C. Tonne, Association between ambient temperature and heat waves with mortality in South Asia: Systematic review and meta-analysis, Environ. Int. 146 (2021), 106170, https://doi.org/10.1016/J.ENVINT.2020.106170.

[4] M. Santamouris, Cooling the buildings – past, present and future, Energy Build. 128 (2016) 617–638, https://doi.org/10.1016/j.enbuild.2016.07.034.

[5] IEA, The Future of Cooling, 2018. https://doi.org/10.1787/9789264301993-en.

[6] C. Delmastro, IEA - Buildings, Paris, 2022. https://www.iea.org/reports/buildings.

[7] International Energy Agency, Technology and innovation pathways for zero-carbon-ready buildings by 2030, 2022. https://www.iea.org/reports/technology-and-innovation-pathways-for-zero-carbon-ready-buildings-by-2030.

[8] M.A.D. Larsen, S. Petrović, A.M. Radoszynski, R. McKenna, O. Balyk, Climate change impacts on trends and extremes in future heating and cooling demands over Europe, Energy Build. 226 (2020), 110397, https://doi.org/10.1016/j.enbuild.2020.110397.

[9] IPCC, Urgent climate action can secure a liveable future for all, (2023). www.ipcc.ch.

[10] U. Berardi, S. Jones, The efficiency and GHG emissions of air source heat pumps under future climate scenarios across Canada, Energy Build. 262 (2022), 112000, https://doi.org/10.1016/J.ENBUILD.2022.112000.

[11] J.L. Fan, J.W. Hu, X. Zhang, Impacts of climate change on electricity demand in China: An empirical estimation based on panel data, Energy. 170 (2019) 880–888, https://doi.org/10.1016/J.ENERGY.2018.12.044.

[12] P. Bezerra, F. da Silva, T. Cruz, M. Mistry, E. Vasquez-Arroyo, L. Magalar, E. De Cian, A.F.P. Lucena, R. Schaeffer, Impacts of a warmer world on space cooling demand in Brazilian households, Energy Build. 234 (2021), 110696, https://doi.org/10.1016/J.ENBUILD.2020.110696.

[13] J. Joshi, A. Magal, V.S. Limaye, P. Madan, A. Jaiswal, D. Mavalankar, K. Knowlton, Climate change and 2030 cooling demand in Ahmedabad, India: opportunities for expansion of renewable energy and cool roofs, Mitig. Adapt. Strateg. Glob. Chang. 27 (2022) 44, https://doi.org/10.1007/S11027-022-10019-4.

[14] M. Sivak, Potential energy demand for cooling in the 50 largest metropolitan areas of the world: Implications for developing countries, Energy Policy. 37 (2009) 1382–1384, https://doi.org/10.1016/J.ENPOL.2008.11.031.

[15] International Energy Agency, Studie: World Energy Outlook 2022, 2022. https://www.iea.org/reports/world-energy-outlook-2022.

[16] India Energy Outlook, India Energy Outlook 2021 – Analysis - IEA, India Energy Outlook. (2021) NA. https://www.iea.org/reports/india-energy-outlook-2021.

[17] S. Attia, R. Levinson, E. Ndongo, P. Holzer, O. Berk Kazanci, S. Homaei, C. Zhang, B.W. Olesen, D. Qi, M. Hamdy, P. Heiselberg, Resilient cooling of buildings to protect against heat waves and power outages: Key concepts and definition, Energy Build. 239 (2021), 110869.

[18] J. Bloomfield, F. Steward, The Politics of the Green New Deal, Polit. Q. 91 (2020) 770–779, https://doi.org/10.1111/1467-923X.12917.

[19] U. Nations, D. of Economic, S. Affairs, P. Division, World Population Prospects 2022: Methodology of the United Nations population estimates and projections, (2022). www.unpopulation.org.

[20] M. Santamouris, Cooling of buildings: The new energy challenge, Cool. Energy Solut. Build. Cities. (2019) 1–16, https://doi.org/10.1142/9789813236974_0001.

[21] C. Mora, B. Dousset, I.R. Caldwell, F.E. Powell, R.C. Geronimo, C.R. Bielecki, C.W. W. Counsell, B.S. Dietrich, E.T. Johnston, L.V. Louis, M.P. Lucas, M.M. Mckenzie, A.G. Shea, H. Tseng, T.W. Giambelluca, L.R. Leon, E. Hawkins, C. Trauernicht, Global Risk of Deadly Heat 7 (2017) 501–506. https://www.nature.com/articles/nclimate3322.

[22] S.L. de Moraes, R. Almendra, L.V. Barrozo, Impact of heat waves and cold spells on cause-specific mortality in the city of São Paulo, Brazil, Int. J. Hyg. Environ. Health. 239 (2022), 113861, https://doi.org/10.1016/J.IJHEH.2021.113861.

[23] A. Barreca, K. Clay, O. Deschenes, M. Greenstone, J.S. Shapiro, Adapting to climate change: The remarkable decline in the US temperature-mortality relationship over the Twentieth Century, J. Polit. Econ. 124 (2016) 105–159, https://doi.org/10.1086/684582.

[24] K.L. Ebi, A. Capon, P. Berry, C. Broderick, R. de Dear, G. Havenith, Y. Honda, R. S. Kovats, W. Ma, A. Malik, N.B. Morris, L. Nybo, S.I. Seneviratne, J. Vanos, O. Jay, Hot weather and heat extremes: health risks, Lancet. 398 (2021) 698–708, https://doi.org/10.1016/S0140-6736(21)01208-3.

[25] A. Nori-Sarma, G.B. Anderson, A. Rajiva, G. ShahAzhar, P. Gupta, M.S. Pednekar, J.Y. Son, R.D. Peng, M.L. Bell, The impact of heat waves on mortality in Northwest India, Environ. Res. 176 (2019), 108546, https://doi.org/10.1016/J.ENVRES.2019.108546.

[26] L. Davis, P. Gertler, S. Jarvis, C. Wolfram, Air conditioning and global inequality, Glob. Environ. Chang. 69 (2021), 102299, https://doi.org/10.1016/J.GLOENVCHA.2021.102299.

[27] T. Randazzo, E. De Cian, M.N. Mistry, Air conditioning and electricity expenditure: The role of climate in temperate countries, Econ. Model. 90 (2020) 273–287, https://doi.org/10.1016/J.ECONMOD.2020.05.001.

[28] R. Galvin, Radically reducing UK energy poverty by the 10% and LIHC indicator through progressive fiscal policy: What would it cost, who would pay, and what are the consequences for CO2 emissions? Sci. Talks. 4 (2022), 100081 https://doi.org/10.1016/J.SCTALK.2022.100081.

[29] C. Chan, L.L. Delina, Energy poverty and beyond: The state, contexts, and trajectories of energy poverty studies in Asia, Energy Res. Soc. Sci. 102 (2023), 103168, https://doi.org/10.1016/J.ERSS.2023.103168.

[30] A. Uwamaliya, A. Jose, A. Wadhwa, B. Hartley, B. Dean, C. Rossi di Schio, S. Mehic, A. Stojanov, E. Ben-Zwi, I. Blanc, J. Nasser, M. Otarra, S. Kennedy, A. Restrepo-Montoya, X. Jin, S. Associate, K. Cooling Efficiency Program, A. Miller, Chilling Prospects: Tracking Sustainable Cooling for All 2022 | Sustainable Energy for All, 2022. https://www.seforall.org/chilling-prospects-2022.

[31] S. Gupta, E. Gupta, G.K. Sarangi, Household Energy Poverty Index for India: An analysis of inter-state differences, Energy Policy. 144 (2020), 111592, https://doi.org/10.1016/J.ENPOL.2020.111592.

[32] B. Bandyopadhyay, M. Banerjee, Decarbonization of cooling of buildings, Sol. Compass. 2 (2022), 100025, https://doi.org/10.1016/J.SOLCOM.2022.100025.

[33] O. Jay, A. Capon, P. Berry, C. Broderick, R. de Dear, G. Havenith, Y. Honda, R. S. Kovats, W. Ma, A. Malik, N.B. Morris, L. Nybo, S.I. Seneviratne, J. Vanos, K. L. Ebi, Reducing the health effects of hot weather and heat extremes: from personal cooling strategies to green cities, Lancet. 398 (2021) 709–724, https://doi.org/10.1016/S0140-6736(21)01209-5.

[34] L. Borghero, E. Clèries, T. Péan, J. Ortiz, J. Salom, Comparing cooling strategies to assess thermal comfort resilience of residential buildings in Barcelona for present and future heatwaves, Build. Environ. 231 (2023), 110043, https://doi.org/10.1016/j.buildenv.2023.110043.

[35] D.K. Bhamare, M.K. Rathod, J. Banerjee, Passive cooling techniques for building and their applicability in different climatic zones—The state of art, Energy Build. 198 (2019) 467–490, https://doi.org/10.1016/J.ENBUILD.2019.06.023.

[36] F. Bazdidi-Tehrani, S. Masoumi-Verki, P. Gholamalipour, Impact of opening shape on airflow and pollutant dispersion in a wind-driven cross-ventilated model building: Large eddy simulation, Sustain. Cities Soc. 61 (2020), 102196, https://doi.org/10.1016/J.SCS.2020.102196.

[37] G. Tognon, M. Marigo, M. De Carli, A. Zarrella, Mechanical, natural and hybrid ventilation systems in different building types: Energy and indoor air quality analysis, J. Build. Eng. 76 (2023), 107060, https://doi.org/10.1016/J.JOBE.2023.107060.

[38] D. Etheridge, A perspective on fifty years of natural ventilation research, Build. Environ. 91 (2015) 51–60, https://doi.org/10.1016/j.buildenv.2015.02.033.

[39] D. Bienvenido-Huertas, C. Rubio-Bellido, A. Pérez-Fargallo, J.A. Pulido-Arcas, Energy saving potential in current and future world built environments based on the adaptive comfort approach, J. Clean. Prod. 249 (2020), 119306, https://doi.org/10.1016/J.JCLEPRO.2019.119306.

[40] N.R.M. Sakiyama, L. Mazzaferro, J.C. Carlo, T. Bejat, H. Garrecht, Natural ventilation potential from weather analyses and building simulation, Energy Build. 231 (2021), 110596, https://doi.org/10.1016/J.ENBUILD.2020.110596.

[41] J.W. Axley, Application of natural ventilation for U.S. commerical buildings : climate suitability design strategies and methods modeling studies, (2001). https://doi.org/10.6028/NIST.GCR.01-820.

[42] Z. Jiang, T. Kobayashi, T. Yamanaka, M. Sandberg, A literature review of cross ventilation in buildings, Energy Build. 291 (2023), 113143, https://doi.org/10.1016/j.enbuild.2023.113143.

[43] H.Y. Zhong, Y. Sun, J. Shang, F.P. Qian, F.Y. Zhao, H. Kikumoto, C. Jimenez-Bescos, X. Liu, Single-sided natural ventilation in buildings: a critical literature review, Build. Environ. 212 (2022), 108797, https://doi.org/10.1016/J.BUILDENV.2022.108797.

[44] P. Heiselberg, Ventilative Cooling Principles, Potential and Barriers, Springer. (2021) 15–37, https://doi.org/10.1007/978-3-030-72385-9_2.

[45] S. Omrani, V. Garcia-Hansen, B.R. Capra, R. Drogemuller, Effect of natural ventilation mode on thermal comfort and ventilation performance: Full-scale measurement, Energy Build. 156 (2017) 1–16, https://doi.org/10.1016/j.enbuild.2017.09.061.

[46] E. Spentzou, M.J. Cook, S. Emmitt, Natural ventilation strategies for indoor thermal comfort in Mediterranean apartments, Build. Simul. 11 (2018) 175–191, https://doi.org/10.1007/S12273-017-0380-1/METRICS.

[47] G. Chiesa, M. Kolokotroni, P. Heiselberg, Innovations in Ventilative Cooling, in: G. Chiesa, M. Kolokotroni, P. Heiselberg (Eds.), Springer, Springer International Publishing, Cham, 2021, pp. 1–12, https://doi.org/10.1007/978-3-030-72385-9_1.

[48] T. Ahmed, P. Kumar, L. Mottet, Natural ventilation in warm climates: The challenges of thermal comfort, heatwave resilience and indoor air quality, Renew. Sustain. Energy Rev. 138 (2021), 110669, https://doi.org/10.1016/J.RSER.2020.110669.

[49] K. Bamdad, S. Matour, N. Izadyar, T. Law, Introducing extended natural ventilation index for buildings under the present and future changing climates, Build. Environ. 226 (2022), 109688, https://doi.org/10.1016/J.BUILDENV.2022.109688.

[50] L. Ledo Gomis, M. Fiorentini, D. Daly, Potential and practical management of hybrid ventilation in buildings, Energy Build. 231 (2021), 110597, https://doi.org/10.1016/j.enbuild.2020.110597.

[51] R. Stasi, F. Ruggiero, U. Berardi, Evaluation of mixed mode ventilation cooling energy saving potential in nZEB: A case study in Southern Italy, E3S Web Conf. 343 (2022) 01004, https://doi.org/10.1051/E3SCONF/202234301004.

[52] G.S. Brager, R.J. De Dear, Thermal adaptation in the built environment: a literature review, Energy Build. 27 (1998) 83–96, https://doi.org/10.1016/S0378-7788(97)00053-4.

[53] R. Stasi, F. Ruggiero, U. Berardi, The efficiency of hybrid ventilation on cooling energy savings in NZEBs, J. Build. Eng. 53 (2022), 104401, https://doi.org/10.1016/j.jobe.2022.104401.

[54] H. Cho, D. Cabrera, S. Sardy, R. Kilchherr, S. Yilmaz, M.K. Patel, Evaluation of performance of energy efficient hybrid ventilation system and analysis of occupants' behavior to control windows, Build. Environ. 188 (2021), 107434, https://doi.org/10.1016/j.buildenv.2020.107434.

[55] Y. Chen, Z. Tong, A. Malkawi, Investigating natural ventilation potentials across the globe: Regional and climatic variations, Build. Environ. 122 (2017) 386–396, https://doi.org/10.1016/j.buildenv.2017.06.026.

[56] W. Li, Q. Chen, Design-based natural ventilation cooling potential evaluation for buildings in China, J. Build. Eng. 41 (2021), 102345, https://doi.org/10.1016/J.JOBE.2021.102345.

[57] D.K. Bhamare, M.K. Rathod, J. Banerjee, Evaluation of cooling potential of passive strategies using bioclimatic approach for different Indian climatic zones, J. Build. Eng. 31 (2020), 101356, https://doi.org/10.1016/J.JOBE.2020.101356.

[58] C. Cen, S. Cheng, N.H. Wong, Effect of elevated air temperature and air velocity on thermal comfort and cognitive performance in the tropics, Build. Environ. 234 (2023), 110203, https://doi.org/10.1016/J.BUILDENV.2023.110203.

[59] M. Bayoumi, Energy saving method for improving thermal comfort and air quality in warm humid climates using isothermal high velocity ventilation, Renew. Energy. 114 (2017) 502–512, https://doi.org/10.1016/J.RENENE.2017.07.056.

[60] F. Nicol, Ventilative Cooling and Comfort Models, Springer. (2021) 39–52, https://doi.org/10.1007/978-3-030-72385-9_3.

[61] X. Jia, J. Wang, Y. Zhu, W. Ji, B. Cao, Cooling effect of elevated ambient air velocity on thermal comfort when sitting after walking, Build. Environ. 225 (2022), 109664, https://doi.org/10.1016/j.buildenv.2022.109664.

[62] W. Yin, G. Zhang, W. Yang, X. Wang, Natural ventilation potential model considering solution multiplicity, window opening percentage, air velocity and humidity in China, Build. Environ. 45 (2010) 338–344, https://doi.org/10.1016/j.buildenv.2009.06.012.

[63] R. Mateus, J.M.C. Pereira, A. Pinto, Natural ventilation of large air masses: Experimental and numerical techniques review, Energy Build. 291 (2023), 113120, https://doi.org/10.1016/j.enbuild.2023.113120.

[64] M. Shirzadi, P.A. Mirzaei, M. Naghashzadegan, Y. Tominaga, Modelling enhancement of cross-ventilation in sheltered buildings using stochastic optimization, Int. J. Heat Mass Transf. 118 (2018) 758–772, https://doi.org/10.1016/J.IJHEATMASSTRANSFER.2017.10.107.

[65] M. Shirzadi, P.A. Mirzaei, Y. Tominaga, CFD analysis of cross-ventilation flow in a group of generic buildings: Comparison between steady RANS, LES and wind tunnel experiments, Build. Simul. 13 (2020) 1353–1372, https://doi.org/10.1007/S12273-020-0657-7/METRICS.

[66] A. Ricci, I. Kalkman, B. Blocken, M. Burlando, M.P. Repetto, Impact of turbulence models and roughness height in 3D steady RANS simulations of wind flow in an urban environment, Build. Environ. 171 (2020), 106617, https://doi.org/10.1016/J.BUILDENV.2019.106617.

[67] S.F. Díaz-Calderón, J.A. Castillo, G. Huelsz, Evaluation of different window heights and facade porosities in naturally cross-ventilated buildings: CFD validation, J. Wind Eng. Ind. Aerodyn. 232 (2023), 105263, https://doi.org/10.1016/J.JWEIA.2022.105263.

[68] H.K. Dai, C. Chen, Air infiltration rates in residential units of a public housing estate in Hong Kong, Build. Environ. 219 (2022), 109211, https://doi.org/10.1016/J.BUILDENV.2022.109211.

[69] P. Stoakes, U. Passe, F. Battaglia, Predicting natural ventilation flows in whole buildings. Part 1: The Viipuri Library, Build. Simul. 4 (2011), https://doi.org/10.1007/s12273-011-0045-4.

[70] Y. Chen, Z. Tong, W. Wu, H. Samuelson, A. Malkawi, L. Norford, Achieving natural ventilation potential in practice: Control schemes and levels of automation, Appl. Energy. 235 (2019) 1141–1152, https://doi.org/10.1016/J.APENERGY.2018.11.016.

[71] D. Bienvenido-Huertas, J.A. Pulido-Arcas, C. Rubio-Bellido, A. Pérez-Fargallo, Feasibility of adaptive thermal comfort for energy savings in cooling and heating: A study on Europe and the Mediterranean basin, Urban Clim. 36 (2021), 100807, https://doi.org/10.1016/J.UCLIM.2021.100807.

[72] R. de Dear, J. Xiong, J. Kim, B. Cao, A review of adaptive thermal comfort research since 1998, Energy Build. 214 (2020), 109893.

[73] A. Yaduvanshi, R. Singh, R. Kumar, Population changes and sustainability of energy drive cooling demand related risks in urbanized India, Energy Build. 260 (2022), 111891, https://doi.org/10.1016/J.ENBUILD.2022.111891.

[74] K. Kosutova, T. van Hooff, C. Vanderwel, B. Blocken, J. Hensen, Cross-ventilation in a generic isolated building equipped with louvers: Wind-tunnel experiments and CFD simulations, Build. Environ. 154 (2019) 263–280, https://doi.org/10.1016/J.BUILDENV.2019.03.019.

[75] N.R.M. Sakiyama, J.C. Carlo, J. Frick, H. Garrecht, Perspectives of naturally ventilated buildings: A review, Renew. Sustain. Energy Rev. 130 (2020), 109933, https://doi.org/10.1016/j.rser.2020.109933.

[76] S. Fan, M.S. Davies Wykes, W.E. Lin, R.L. Jones, A.G. Robins, P.F. Linden, A full-scale field study for evaluation of simple analytical models of cross ventilation and single-sided ventilation, Build. Environ. 187 (2021), 107386, https://doi.org/10.1016/J.BUILDENV.2020.107386.

[77] T. van Hooff, B. Blocken, Full-scale measurements of indoor environmental conditions and natural ventilation in a large semi-enclosed stadium: Possibilities and limitations for CFD validation, J. Wind Eng. Ind. Aerodyn. 104–106 (2012) 330–341, https://doi.org/10.1016/J.JWEIA.2012.02.009.

[78] Z. Zhiyi, Y. Wei, W. Tianwen, L. Yonghan, Z. Yawen, Z. Guoqiang, Potential of cross-ventilation channels in an ideal typical apartment building predicted by CFD and multi-zone airflow model, J. Build. Eng. 44 (2021), 103408, https://doi.org/10.1016/J.JOBE.2021.103408.

[79] P.V. Nielsen, F. Allard, H.B. Awbi, L. Davidson, A. Schälin, Computational Fluid Dynamics in Ventilation Design REHVA Guidebook No 10, Int. J. Vent. 6 (2007) 291–294, https://doi.org/10.1080/14733315.2007.11683784.

[80] B. Blocken, 50 years of Computational Wind Engineering: Past, present and future, J. Wind Eng. Ind. Aerodyn. 129 (2014) 69–102, https://doi.org/10.1016/J.JWEIA.2014.03.008.
[81] A. Aflaki, M. Esfandiari, S. Mohammadi, A Review of Numerical Simulation as a Precedence Method for Prediction and Evaluation of Building Ventilation Performance, Sustain. 2021, Vol. 13, Page 12721. 13 (2021) 12721. https://doi.org/10.3390/SU132212721.
[82] M. Rodríguez-Vázquez, I. Hernández-Pérez, J. Xamán, Y. Chávez, M. Gijón-Rivera, J.M. Belman-Flores, Coupling building energy simulation and computational fluid dynamics: An overview, J. Build. Phys. 44 (2020) 137–180, https://doi.org/10.1177/1744259120901840.
[83] C. India, Government of India, Census of India, Government of India, (2011).
[84] S. Kumar, S. Kachhawa, A. Goenka, S. Kasamsetty, G. George, Demand analysis for cooling by sector in India in 2027, Bur. Energy Effic. Minist. Power, Govt. India. (2018) Alliance for an Energy Efficient Economy. www.aeee.in.
[85] R. de Dear, The Theory of Thermal Comfort in Naturally Ventilated Indoor Environments - "The Pleasure Principle," Http://Dx.Doi.Org/10.1080/14733315.2009.11683849. 8 (2016) 243–250. https://doi.org/10.1080/14733315.2009.11683849.
[86] G. Betti, F. Tartarini, C. Nguyen, S. Schiavon, CBE Clima Tool: a free and open-source web application for climate analysis tailored to sustainable building design, (2022). https://doi.org/10.48550/arxiv.2212.04609.
[87] J.I. Perén, T. van Hooff, R. Ramponi, B. Blocken, B.C.C. Leite, Impact of roof geometry of an isolated leeward sawtooth roof building on cross-ventilation: Straight, concave, hybrid or convex? J. Wind Eng. Ind. Aerodyn. 145 (2015) 102–114, https://doi.org/10.1016/j.jweia.2015.05.014.
[88] B. Blocken, J. Carmeliet, T. Stathopoulos, CFD evaluation of wind speed conditions in passages between parallel buildings—effect of wall-function roughness modifications for the atmospheric boundary layer flow, J. Wind Eng. Ind. Aerodyn. 95 (2007) 941–962, https://doi.org/10.1016/J.JWEIA.2007.01.013.
[89] J.I. Perén, T. van Hooff, B.C.C. Leite, B. Blocken, CFD simulation of wind-driven upward cross ventilation and its enhancement in long buildings: Impact of single-span versus double-span leeward sawtooth roof and opening ratio, Build. Environ. 96 (2016) 142–156, https://doi.org/10.1016/J.BUILDENV.2015.11.021.
[90] R. Ramponi, B. Blocken, CFD simulation of cross-ventilation for a generic isolated building: Impact of computational parameters, Build. Environ. 53 (2012) 34–48, https://doi.org/10.1016/J.BUILDENV.2012.01.004.
[91] B. Wang, A. Malkawi, Design-based natural ventilation evaluation in early stage for high performance buildings, Sustain. Cities Soc. 45 (2019) 25–37, https://doi.org/10.1016/j.scs.2018.11.024.
[92] D. Mohotti, K. Wijesooriya, D. Dias-da-Costa, Comparison of Reynolds Averaging Navier-Stokes (RANS) turbulent models in predicting wind pressure on tall buildings, J. Build. Eng. 21 (2019) 1–17, https://doi.org/10.1016/J.JOBE.2018.09.021.
[93] B.E. Launder, D.B. Spalding, The numerical computation of turbulent flows, Comput. Methods Appl. Mech. Eng. 3 (1974) 269–289, https://doi.org/10.1016/0045-7825(74)90029-2.
[94] T. Cebeci, P. Bradshaw, Momentum transfer in boundary layers, Hemi. (1977). https://ui.adsabs.harvard.edu/abs/1977hemi.book....C/abstract.
[95] Q. Chen, J. Srebric, A procedure for verification, validation, and reporting of indoor environment CFD analyses, HVAC R Res. 8 (2002) 201–216, https://doi.org/10.1080/10789669.2002.10391437.
[96] M. Karimimoshaver, M. Sadathosseini, F. Aram, J. Ahmadi, A. Mosavi, The effect of geometry and location of balconies on single-sided natural ventilation in high-rise buildings, Energy Reports. 10 (2023) 2174–2193, https://doi.org/10.1016/J.EGYR.2023.09.030.
[97] P. Karava, Airflow Prediction in Buildings for Natural Ventilation Design, Wind Tunnel Measurements and Simulation-TEZ (2008).
[98] Ashrae, ANSI/ASHRAE Standard 55-2020, 2021. www.ashrae.org.
[99] S. Carlucci, L. Bai, R. de Dear, L. Yang, Review of adaptive thermal comfort models in built environmental regulatory documents, Build. Environ. 137 (2018) 73–89, https://doi.org/10.1016/J.BUILDENV.2018.03.053.
[100] R. Yao, S. Zhang, C. Du, M. Schweiker, S. Hodder, B.W. Olesen, J. Toftum, F. Romana d'Ambrosio, H. Gebhardt, S. Zhou, F. Yuan, B. Li, Evolution and performance analysis of adaptive thermal comfort models – A comprehensive literature review, Build. Environ. 217 (2022), 109020, https://doi.org/10.1016/J.BUILDENV.2022.109020.
[101] R. Rawal, Y. Shukla, V. Vardhan, S. Asrani, M. Schweiker, R. de Dear, V. Garg, J. Mathur, S. Prakash, S. Diddi, S.V. Ranjan, A.N. Siddiqui, G. Somani, Adaptive thermal comfort model based on field studies in five climate zones across India, Build. Environ. 219 (2022), 109187, https://doi.org/10.1016/J.BUILDENV.2022.109187.
[102] S. Manu, Y. Shukla, R. Rawal, L.E. Thomas, R. de Dear, Field studies of thermal comfort across multiple climate zones for the subcontinent: India Model for Adaptive Comfort (IMAC), Build. Environ. 98 (2016) 55–70, https://doi.org/10.1016/J.BUILDENV.2015.12.019.
[103] S. Carlucci, S. Erba, L. Pagliano, R. de Dear, ASHRAE Likelihood of Dissatisfaction: A new right-here and right-now thermal comfort index for assessing the Likelihood of dissatisfaction according to the ASHRAE adaptive comfort model, Energy Build. 250 (2021), 111286, https://doi.org/10.1016/J.ENBUILD.2021.111286.
[104] S. Carlucci, A review of long-term discomfort indices, SpringerBriefs Appl, Sci. Technol. (2013) 1–20, https://doi.org/10.1007/978-88-470-5238-3_1.
[105] S. Carlucci, L. Pagliano, A. Sangalli, Statistical analysis of the ranking capability of long-term thermal discomfort indices and their adoption in optimization processes to support building design, Build. Environ. 75 (2014) 114–131, https://doi.org/10.1016/J.BUILDENV.2013.12.017.
[106] J. Malik, R. Bardhan, A localized adaptive comfort model for free-running low-income housing in Mumbai, India, Energy Build. 281 (2023), 112756, https://doi.org/10.1016/J.ENBUILD.2022.112756.
[107] I. Siksnelyte-Butkiene, D. Streimikiene, V. Lekavicius, T. Balezentis, Energy poverty indicators: A systematic literature review and comprehensive analysis of integrity, Sustain. Cities Soc. 67 (2021), 102756, https://doi.org/10.1016/J.SCS.2021.102756.
[108] UNDP. 2023 https://www.undp.org/india/publications/national-multidimensional-poverty-index-progress-review-2023.
[109] N. Nasrollahi, P. Ghobadi, Field measurement and numerical investigation of natural cross-ventilation in high-rise buildings; Thermal comfort analysis, Appl. Therm. Eng. 211 (2022), 118500, https://doi.org/10.1016/J.APPLTHERMALENG.2022.118500.
[110] P. Karava, T. Stathopoulos, A.K. Athienitis, Airflow assessment in cross-ventilated buildings with operable façade elements, Build. Environ. 46 (2011) 266–279, https://doi.org/10.1016/J.BUILDENV.2010.07.022.